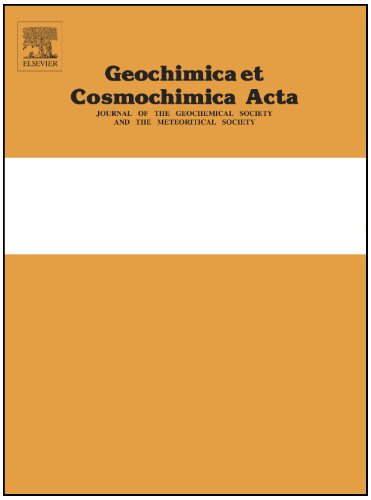

Geochimica et Cosmochimica Acta

JOURNAL OF THE GEOCHEMICAL SOCIETY AND THE METEORITICAL SOCIETY

Constraining carbonate diagenesis using clumped isotope temperatures and U-Pb dating: A case study and implications for paleoelevation interpretations in western central Tibet

Lin Li, Peter DeCelles, Paul Kapp, Carmala Garzione, Jay Quade, Nitzan Yanay

PII: S0016-7037(24)00176-5
DOI: https://doi.org/10.1016/j.gca.2024.04.007
Reference: GCA 13379

To appear in: *Geochimica et Cosmochimica Acta*

Received Date: 23 June 2023
Accepted Date: 4 April 2024

Please cite this article as: Li, L., DeCelles, P., Kapp, P., Garzione, C., Quade, J., Yanay, N., Constraining carbonate diagenesis using clumped isotope temperatures and U-Pb dating: A case study and implications for paleoelevation interpretations in western central Tibet, *Geochimica et Cosmochimica Acta* (2024), doi: https://doi.org/10.1016/j.gca.2024.04.007

Constraining carbonate diagenesis using clumped isotope temperatures and U-Pb dating: a case study and implications for paleoelevation interpretations in western central Tibet

Lin Li[1,*], Peter DeCelles[1], Paul Kapp[1], Carmala Garzione[1], Jay Quade[1], Nitzan Yanay[1]

[1]Department of Geosciences, University of Arizona, Tucson, AZ 85721, USA

Corresponding author email: linli2@arizona.edu

Abstract

Carbonate rocks are susceptible to diagenesis, and the correct identification of diagenetic features and stages are primary tasks in paleoelevation and paleoclimate studies using carbonate proxies. In this study, we apply three key parameters that include stable isotopes, clumped isotope temperatures, and U-Pb ages to identify different diagenetic stages, i.e., eogenesis, mesogenesis, and telogenesis. We then adopt these criteria to explore the diagenetic history of the middle–late Eocene lacustrine carbonates in the Gerze area of western central Tibet, which have yielded contrasting interpretations of diagenetic stages and paleoelevation estimates. Petrographic observations and electron microprobe element mapping permitted the identification of different diagenetic features. The Gerze carbonates (4GZ section) contain distinct phases of micrite and vein/vug-fill calcite (sparite) with different stable oxygen isotope values of -4 to -6‰ and -10 to -14‰ (VPDB), respectively. The micrites are dominantly dolomite in composition and yield clumped isotope temperatures of 40–50 °C, which are interpreted to be the result of dolomitization during shallow burial. In contrast, the vein/vug-fill calcites exhibit lower clumped isotope temperatures of 20–30 °C and U-Pb ages of 3.0–3.3 Ma, indicating a late-stage telogenetic origin after exhumation to near the Earth's surface. Our documentation of different carbonate diagenetic stages sheds light on existing paleoelevation interpretations. We conclude that existing evidence remains inconclusive as to the paleoelevation of the Gerze area basin floors during the middle–late Eocene.

Keywords:

Central Tibet, lacustrine carbonate, EPMA, dolomitization, telogenesis, paleoelevation

1. Introduction

Stable isotope-based paleoaltimetry (Chamberlain and Poage, 2000; Garzione et al., 2000; Rowley and Garzione, 2007; Rowley et al., 2001) has proven to be a powerful tool for understanding the processes and drivers that have contributed to the formation and expansion of large orogenic belts and plateaus (e.g., Ding et al., 2022; Garzione et al., 2017; Quade et al., 2015). There is an ongoing debate regarding the paleoelevation evolution of the Bangong suture zone in central Tibet (Fig. 1A), which is critical information for understanding the topographic growth history of the broader Tibetan Plateau and exploring geodynamic processes that have driven the building of large orogenic plateaus in general (Ingalls et al., 2020; Li, L. et al., 2022).

Carbonate stable isotope-based paleoelevation studies in the Lunpola Basin along the Bangong suture zone in central Tibet (Fig. 1A) suggest paleoelevations of ~4 km had been attained in this region by the middle–late Eocene (Ingalls et al., 2020; Polissar et al., 2009; Rowley and Currie, 2006), whereas estimates based on fossil fauna and flora using either coexistence of nearest living relatives or foliar physiognomy methods yield significantly lower values of 1.0–2.3 km elevation in both the Lunpola and nearby Nima basins (Fig. 1A) for the same period (Cai et al., 2019; Su et al., 2019; Su et al., 2020; Wu et al., 2017). A more recent carbonate clumped isotope temperature study has also suggested a paleoelevation of <2 km for the middle–late Eocene Lunpola Basin (Xiong et al., 2022). These discrepancies clearly suggest that further studies are required to resolve the question of the paleoelevation of the Bangong suture zone during the middle–late Eocene.

The Gerze area, situated in the western segment of the Bangong suture zone (Fig. 1A), contains middle–upper Eocene strata with lacustrine carbonates. A paleoelevation study of the area (Fig. 1C), using stable oxygen isotopes ($\delta^{18}O_{carb}$) of lacustrine carbonate and vein/vug-fill calcite, revealed two distinctive groups of $\delta^{18}O_{carb}$ values (Wei et al., 2016). The low $\delta^{18}O_{carb}$ values (-11.0 ± 4.0 ‰, VPDB) of vein/vug-fill calcite (sparite) were attributed to either carbonate precipitation from meteoric water, consistent with modern high-altitude water, or precipitation at burial depths where temperatures are higher than the surface (Wei et al., 2016). In contrast, the more positive $\delta^{18}O_{carb}$ values (-5.1 ± 1.1 ‰) of lacustrine micrite were considered to represent the primary isotopic values of an open lake at low paleoelevations (Wei et al., 2016). Results of this study and from the Lunpola and Nima basins (Cai et al., 2019; Su et al., 2019; Su et al., 2020; Wu et al., 2017) imply the existence of an east-west trending low-elevation valley in central Tibet during the middle–late Eocene, becoming broader in width and lower in elevation westward (Li, L. et al., 2022). However, the interpretation of Wei et al. (2016) has been challenged by Ingalls et al. (2020), who suggested that the elevated $\delta^{18}O_{carb}$ values in micrite could be attributed to a closed lake experiencing evaporation, while the lower $\delta^{18}O_{carb}$ values of vein/vug-fill calcite might have formed during early diagenesis and cementation, and therefore, represent the isotopic values of primary surface meteoric waters at high paleoelevations.

Carbonate is susceptible to diagenesis (Armenteros, 2010; Swart, 2015). It is crucial to differentiate between different diagenetic stages (Fig. 2), i.e., eogenesis (early diagenesis), mesogenesis (deep burial diagenesis), and telogenesis (late stage diagenesis) (Choquette and

Pray, 1970), as processes during these different stages can have varying effects on the primary isotopic signals of carbonates, on which paleoclimate and paleoelevation interpretations are based (e.g., Quade et al., 2020). Studies have demonstrated that carbonates can retain micritic textures despite undergoing mesogenesis, i.e., cryptic-recrystallization (Ingalls, 2019; Lacroix and Niemi, 2019; Shenton et al., 2015). Therefore, it is essential to consider additional objective parameters, other than simply visual determination of micritic textures, to distinguish between these different diagenetic stages. Recent advances in carbonate LA-ICPMS U-Pb dating (Li et al., 2014; Roberts et al., 2020) and clumped isotope thermometry (Eiler and Schauble, 2004; Ghosh et al., 2006) enable direct measurement of carbonate formation ages and temperatures, which offer promising tools for identification of carbonate diagenesis (e.g., Cong et al., 2021; Gasparrini et al., 2023; Mangenot et al., 2018). Fig. 2 presents three criteria that can be used to characterize different carbonate diagenetic stages. Although any single criterion yields ambiguous interpretations, their combination has the potential to yield an explicit result.

To determine whether the Gerze area was at low or high elevations during the middle–late Eocene, it is crucial to determine whether the micrite stable isotope values record the lake water composition during deposition, as well as to establish the timing and environment of vein/vug-fill calcite formation, i.e., whether it formed during early diagenesis, burial diagenesis, or at a later stage of diagenesis. This study aims to provide additional insight into the carbonate diagenetic history and independent paleoelevation estimates by reporting new stable isotope and clumped isotope temperatures of both micrite and vein/vug-fill calcite, X-ray diffraction (XRD) mineralogy, electron probe micro-analysis (EPMA) element mapping, and carbonate LA-ICPMS U-Pb dating of the Gerze area middle–upper Eocene lacustrine carbonates. Finally, we discuss the implications to previous paleoelevation estimates for the middle–late Eocene Gerze area.

2. Geologic setting

2.1 Regional geology

The studied Gerze area is located in the western segment of the Bangong suture zone, which marks the collisional trace between the Lhasa and Qiangtang terranes in central Tibet (Fig. 1A). The timing of the Lhasa-Qiangtang collision is debated, with estimates ranging from the early Late Jurassic, to Late Jurassic–Early Cretaceous, and to early Late Cretaceous (see reviews in Hu et al., 2022; Li, S. et al., 2019). Some of the disparity might be attributed to the east–west diachroneity of the Lhasa-Qiangtang collision (Li, L. et al., 2019; Yin and Harrison, 2000).

In the Gerze area, ophiolitic and deep marine turbiditic rocks of the Bangong suture zone are bounded by the north-dipping Shiquanhe-Gerze-Amdo thrust (SGAT) system on the north, and the south-dipping Gerze-Seling Co backthrust (GSBT) on the south (Fig. 1A–B) (Kapp et al., 2005; Li, S. et al., 2019). Depositional ages of syn-tectonic strata and low-temperature thermochronologic data suggest that both thrust systems were active, albeit possibly intermittently, throughout Cretaceous–Paleogene time, with limited activity during the Neogene (Kapp et al., 2007; Li, C. et al., 2022; Tong et al., 2022). East–west extension, accommodated by normal faults and kinematically linked strike-slip faults initiated by ~10 Ma in the region (Sundell et al., 2013; Woodruff Jr et al., 2013).

2.2 Stratigraphy

Carbonate rocks studied in this research were collected from three detailed measured sedimentary sections from the Gerze area (Supplementary Fig. S1). Sections 2GZ and 3GZ are situated within the Bangong suture zone in the footwall of the GSBT, and section 4GZ is in the hanging wall of the GSBT in the northern Lhasa terrane (Fig. 1B).

Section 2GZ is 425 m thick and consists of an overall upward fining succession of sandstone and mudstone (Supplementary Fig. S1). Sandstone beds are dominated by ripple cross-laminations, with subordinate amounts of massive, trough cross-stratified, and horizontally laminated sandstone. Bioturbation and fragmental fossil bone material are locally abundant. Intervals of red, pink, orange, and maroon-colored mudstone are generally massive but locally laminated. Paleosols (mainly mottled gleysols) are present between the ~110 and 200 m levels. We interpret section 2GZ as the deposits of a fluvial to shallow lacustrine system.

Section 3GZ is 242 m thick and is divisible into a lower 100 m thick interval dominated by conglomerate, a middle 95 m thick interval composed mostly of mudstone, and a 48 m thick upper interval composed mainly of sandstone (Supplementary Fig. S1). Conglomeratic lithofacies in the lower interval consist of clast-supported, massive, horizontally stratified, and imbricated pebble to cobble conglomerate beds that range in thickness from ~50 cm to several meters. Conglomerate clasts consist of limestone, sandstone, siltstone, volcanic rocks, and metabasite. The conglomeratic interval grades upward into the mudstone-rich interval, with interbedded upward fining conglomerates and calcic red paleosols. The mudstone-rich interval contains at least four 1–3 m thick micritic marl beds. The bulk of the interval is massive red siltstone. The upper sandstone-rich interval consists of 30–150 cm thick beds of rippled and horizontally laminated fine-grained sandstone, intercalated with massive red siltstone. Several of the thicker sandstone units fine-upward and have trough cross-stratification in their lower coarser-grained parts. The conglomeratic part of the section is interpreted as alluvial-fan deposits, and the upper two-thirds of the section was probably deposited in a fluvial-lacustrine setting.

Section 4GZ is 105 m thick and consists predominately of fine-grained lithofacies. The section is structurally overturned. Unlike the other sections, 4GZ is dominated by lacustrine deposits, including >20 distinctive light-gray marl beds, typically 20–150 cm thick. The marl beds are well laminated; algal laminae and stromatolites are present in some beds. Organic-rich laminae impart a "paper shale" texture to some of the marl beds. The marls are generally separated by laminated red siltstone/claystone. The base of the section is occupied by a 2-m-thick bed of trough cross-stratified cobble conglomerate composed of mainly limestone clasts. A few calcic paleosols are present in the upper part of the section.

2.3 Age constraints

Based on detrital zircon U-Pb ages (providing a ~42 Ma maximum depositional age constraint), index fossils, and magnetostratigraphy, Wei et al. (2016) dated the deposition in the 4GZ section area between 39.4 and 35.7 Ma. The 4GZ section and Wei et al. (2016)'s section are on opposite limbs of a syncline, and our sampled 4GZ section corresponds to the upper part of Wei et al. (2016)'s section (Fig. 1C). As such, we consider our 4GZ section as early late Eocene in age, ~38–36 Ma.

In the 2GZ and 3GZ sections area, the Meisu volcanic rocks (*Tv*) sitting on top of these sections (Fig. 1B) were dated to be 37–39 Ma (Zhang et al., 2018), indicating that the 2GZ and 3GZ sections must be older than 37 Ma. Our unpublished detrital zircon U-Pb dating indicates that the maximum depositional ages of the 2GZ and 3GZ sections are ~42 Ma (mean of youngest 2 grains; data to be published in a separate manuscript). These ages indicate that the 2GZ and 3GZ sections were deposited between 42 and 37 Ma, similar to the 4GZ section.

3. Methods

3.1 Samples

Seven lacustrine micrite (marl) and one calcified fossil plant were selected for detailed isotopic and mineralogical studies, including one sample from the 2GZ section, two samples from the 3GZ section, and five samples from the 4GZ section (Supplementary Fig. S1). Some of the micrite samples exhibit vein calcite and/or vug-fill calcite. We drilled both micrite and vein/vug-fill calcite for stable and clumped isotope analysis.

3.2 Petrographic and mineralogical analysis

Petrographic thin sections of all samples were observed under a microscope using both plane- and cross-polarized light. Further, all samples were powdered for X-ray diffraction (XRD) experiments at the XRD facility in the Department of Chemistry and Biochemistry of the University of Arizona, on a Philips PANalytical X'Pert PRO MPD instrument. The X-ray radiation wavelength was ~1.54 Angstroms (Å) (copper Ka radiation generated by a sealed X-ray tube with copper anode), and the Bragg-Brentano theta-theta geometry was used in the measurements. Samples were scanned from 10° to 70° 2θ at 0.017° steps. Semiquantitative estimates of the weight percentage (wt%) of each presenting mineral were estimated using the reference intensity ratio (RIR) available in the XRD database. The wt% is proportional to the (XRD intensity)/RIR. All wt% values were then normalized in such a way that the sum of all entries equals 100%.

3.3 EPMA element mapping

Selected thin sections were finely polished and carbon coated for EPMA analysis at the Kuiper Imaging Facility at the University of Arizona using a Cameca SX-100 Ultra instrument. For all element maps, the instrument was configured to 15kV and 40nA. The Mg, Ca, Mn, Sr, and Fe elements were collected using the WDS spectrometers; while the Si, Cr, Ba, and sometimes Mo elements were collected using the EDS spectrometer. For the high-resolution element maps, we used 1024 pixels per line, 40 mm beam size, and 10ms dwell time; for the medium-resolution element maps, we used 512 pixels per line, 80 mm beam size, and 20ms dwell time.

3.4 Carbonate stable isotope analysis

Carbonate stable oxygen ($\delta^{18}O_{carb}$) and carbon ($\delta^{13}C_{carb}$) isotope analyses were carried out at the Environmental Isotope Laboratory at the University of Arizona. We drilled both micrite and vein/vug-fill calcite. Stable isotope data of the drilled carbonate materials were measured using a Finnigan MAT 252 isotope ratio mass spectrometer coupled with a KIEL-III device. NBS-18 and NBS-19 were used as analytical references. Both $\delta^{18}O_{carb}$ and $\delta^{13}C_{carb}$ values are reported with respect to Vienna Peedee belemnite (VPDB).

3.5 Carbonate clumped isotope analysis

About 2 mg of powdered carbonate was reacted with dehydrated phosphoric acid under vacuum at 70 °C. The conventional isotope ratio measurement relative to VPDB was calibrated based on repeated measurements of International Atomic Energy Agency (IAEA) reference materials. Clumped isotope values (Δ_{638}) are reported in the carbon dioxide equilibrium scale (CDES) theoretical reference frame defined by water-equilibrated gases, heated gases, and ETH 1–4 carbonate standards (Bernasconi et al., 2021; Dennis et al., 2011). The Δ_{638} notation refers to measurements using a tunable infrared laser differential spectrometer (TILDAS), performed at the Environmental Isotope Laboratory at the University of Arizona. The precisions for these measurements are ±0.021‰ for Δ_{638}, ±0.04‰ for $\delta^{18}O_{carb}$, and ±0.03‰ for $\delta^{13}C_{carb}$ (pooled reproducibility, 1-sigma), respectively. The laser-based Δ_{638} – temperature relationship for carbonates at relatively low temperatures is based on 44 synthetic calcites that equilibrated at temperatures from 6 °C to 70 °C (Yanay et al., 2022):

$$\Delta_{638CDES} = (0.0405 \pm 0.0006) \times (10^6/T^2) + (0.1822 \pm 0.0061),\ R^2 = 0.985 \qquad (1)$$

Temperature estimates using laser-based Δ_{638} and mass spectrometry-based Δ_{47} measurements have been shown to be statistically equivalent (Yanay et al., 2022). Equation (1) is within error of recent mass spectrometry-based Δ_{47} – temperature relationships and correctly predicted precipitation temperatures for a suite of 17 natural carbonates for both calcite and aragonite (Yanay et al., 2022). Complete details of this method and the calibration of the Δ_{638} – temperature relationship are described in Wang et al. (2020) and Yanay et al. (2022).

All clumped isotope samples were analyzed for 5–7 replicates. Each replicate measurement is based on four comparisons (sub-cycles) of the sample and reference gas. We exclude replicates with fewer than two sub-cycles and outliers to calculate the mean value of each sample. The outlier is defined as follows: first, we calculated the average Δ_{638} value of all replicates for each sample, then we calculated the difference of Δ_{638} between each replicate with the average, and then we considered differences >0.021 ($\Delta_{638CDES}$ external standard deviation of references) as outliers, which corresponds to ~7 °C $T_{(\Delta638)}$ temperatures in the range of 5–70 °C. Most reported clumped isotope values were averaged from four or five accepted replicates, with a few averaged from three replicates. Supplementary Data S1 provides whole clumped isotope data, including excluded replicates, of all unknown samples; Supplementary Data S2 lists whole clumped isotope data of all references (carbonate standards ETH1–4 and equilibrium gas) used for calibration.

The $\delta^{18}O_w$ values of water in which carbonates precipitated were calculated from the clumped isotope temperatures and $\delta^{18}O_{carb}$ values using a linear combination of the dolomite calibration of Vasconcelos et al. (2005): $10^3\ln\alpha_{(dolomite\text{-}water)} = (2.73 \times 10^6)/(T + 273.15)^2 + 0.26$; and calcite calibration of Kim and O'Neil (1997): $10^3\ln\alpha_{(calcite\text{-}water)} = (18.03 \times 10^3)/(T + 273.15) - 32.42$. The relative abundance of calcite and dolomite is based on X-ray diffraction results.

3.6 Solid-state reordering modeling

Carbonate may experience solid-state reordering and associated changes in clumped isotope values when buried to higher temperatures (>~130–150 °C) for a certain period of time (millions of years) (Hemingway and Henkes, 2021; Henkes et al., 2014; Lloyd et al., 2018; Passey and Henkes, 2012; Stolper and Eiler, 2015). To evaluate the potential influence of solid-state reordering on carbonate clumped isotope temperatures, we used the Isotopylog package for Python (version 0.0.8, released on May 24, 2023) and parameters for either calcite or dolomite of Hemingway and Henkes (2021a). This model is chosen as it has been shown theoretically that all previous models (e.g., Henkes et al., 2014; Stolper and Eiler, 2015) are specific cases of the new model Hemingway and Henkes (2021a). We note that the most recent version of the Isotopylog package yields results that are different from the original version i.e., higher maximum burial temperatures and longer duration of maximum burial are needed to reorder calcite/dolomite to a specific temperature. See Hemingway and Henkes (2021b) for a discussion of the differences and causes.

We conducted two groups of reordering models to figure out the maximum temperatures (burial depth) needed to reorder dolomite or calcite minerals from 30°C to 50°C. The first group of modeling is for the dolomitic micrite of section 4GZ, and the other group is for the vein/vug-fill calcite of sections 2GZ and 3GZ. As we have no other constraints for the burial and exhumation history, such as vitrinite reflectance and/or low-temperature thermochronology data for all three sections, we assumed the following scenario: carbonate formed at a temperature of 30 °C at 38 Ma, was gradually buried to maximum depth (a value that we try to figure out from the reordering modeling) at 20 Ma, stayed at maximum depth until ~5 Ma, and then experienced fast exhumation to the Earth surface at ~3 Ma (constrained by carbonate U-Pb ages of 4GZ vein/vug-fill calcite, considering that they were formed near Earth's surface after exhumation, see section 4.6).

To evaluate the influence of different burial and exhumation scenarios on reordering results, we also tested the reordering models assuming two other different burial and exhumation scenarios, assuming different timing to reach maximum burial (20 *vs.* 30 Ma) and duration of maximum burial (e.g., 10 *vs.* 5 Myrs). Additional reordering modeling was carried out to figure out the reordered temperatures of dolomite (calcite) under the maximum burial temperatures that can reorder 30 °C calcite (dolomite) to 50 °C.

3.7 Carbonate LA-ICP-MS U-Pb dating

Carbonate U-Pb analyses were performed at the University of California, Santa Barbara using a Photon Machines Excite 193 laser ablation system coupled to a Nu Instruments Plasma 3D multi-collector ICP-MS, following the analytical procedures of Kylander-Clark (2020). Samples were analyzed in polished, one-inch epoxy mounts, using an 85 µm spot run at 10 Hz for 15 s following a 20 s baseline. Unknown analyses were corrected for instrument drift and mass bias in a two-step procedure using a combination of analyses from NIST614 glass and calcite standard WC-1 (254 Ma; Roberts et al., 2017) that were measured periodically throughout the analytical session; NIST614 was first used to correct for instrument drift of all isotopic ratios and the mass and detector bias of the ^{207}Pb/^{206}Pb ratio using Iolite v2.5 (Paton et al., 2011), and a correction for the mass and detector bias of the ^{206}Pb/ ^{238}U ratio was corrected such that, using an initial ^{207}Pb/^{206}Pb ratio of 0.85, WC-1 yields 254 Ma. Analyses of calcite standards ASH 15D (2.965 Ma; Nuriel et al., 2021) and Duff Brown Tank (64 Ma; Hill et al., 2016) throughout the analytical session yielded ages that overlap within uncertainties of their accepted values. All data are presented in Supplementary Data S3.

4. Results

4.1 Petrographic and mineralogical results

Petrographic observations indicate that all carbonate samples in this study contain both micrite and sparry vein/vug-fill calcite, although their proportions differ among the samples (Fig. 3). Specifically, samples 4GZ11, 4GZ18, and 4GZ79 are predominantly micrite, with limited presence of vein/vug-fill calcite (Fig. 3A–C), whereas samples 4GZ7 and 4GZ96 contain abundant vein/vug-fill calcite, constituting approximately one-third to one-half of the thin-section area (Fig. 3D–E). Carbonate samples from the 3GZ section contain a moderate amount of vein/vug-fill calcite (Fig. 3F–G). Additionally, sample 2GZ58 is a fossil, displaying circular sparite cells surrounded by a micrite matrix (Fig. 3H).

Vug-fill calcite and vein calcite may form in different depositional and/or structural environments and at different times (Lacroix et al., 2011; Roberts and Holdsworth, 2022). However, we infer that the relatively large and pure calcite crystals in our vein and vug-fill calcite samples in the 4GZ section formed in the same general setting and time given their similar stable and clumped isotope values (see Sections 4.3 and 4.4 below for details).

XRD analysis of carbonate samples from the 4GZ section revealed two distinct mineralogic patterns (Table 1). Samples 4GZ11, 4GZ18, and 4GZ79 are dominated by dolomite (92–98%). In contrast, samples 4GZ7 and 4GZ96 contain subequal amounts of dolomite and calcite. Based on petrographic observations, we interpret the higher calcite content in these two samples to be a result of contribution from vein/vug-fill calcite. The pervasive distribution and small size of the calcite veins and vugs in these samples (Fig. 3D–E) inevitably result in some amount of vein/vug-fill calcite material being incorporated into the XRD powder during preparation.

4.2 EPMA element maps

The EPMA element maps provide additional evidence to support the petrographic and mineralogical observations. The element maps of sample 4GZ11 show homogeneous Ca and Mg distributions on a coarse scale (Fig. 4A–B), which is consistent with its dominantly dolomite mineralogy identified from XRD. The bottom left area that is dominated by Ca (red color; Fig. 4A) but with no Mg (black color; Fig. 4B) indicates the presence of vein/vug-fill calcite. As expected, the coarse-scale element maps of sample 4GZ96 also show both homogeneous and random patterns of Ca and Mg, but with much more pervasive calcite veins and vugs (Fig. 4C–D). On a much finer-scale element map of sample 4GZ96, the Ca map still shows a homogeneous and random pattern (Fig. 4E), whereas the Mg map of the micrite shows a homogeneous but directional pattern (Fig. 4F), which does not parallel depositional laminations. It is possible that this unusual directional elemental pattern represents pressure-solution seams (Nenna and Aydin, 2011), although it is beyond the scope of this study and more observations are needed to verify this explanation.

In addition to the Ca and Mg element maps, the Si map clearly detects quartz grains, although with small percentages (<5%, Supplementary Figs. S2–S4). Other elements such as Fe, Ti, Sr, Cr, and Ba show homogeneously dull images with no observable differences between micrites and vein/vug-fill calcites (Supplementary Figs. S2–S4). This may indicate no geochemical differences between the two fluids from which the micrites and vein/vug-fill calcites were deposited, or it could be due to low concentrations of these elements beyond the detection limit of EPMA, i.e., <30 ppm. We favor the second explanation, as will be shown below by the LA-ICPMS trace element analysis of U and Th (section 4.6), which does show element concentration differences between micrites and vein/vug-fill calcites.

4.3 Carbonate stable isotope data

The stable oxygen isotope values of carbonate ($\delta^{18}O_{carb}$) show distinct differences between micrites and vein/vug-fill calcites in the 4GZ section: the $\delta^{18}O_{carb}$ values (VPDB) are between -4.5‰ and -6.4‰ for micrites, and between -10.2‰ and -13.9‰ for vein/vug-fill calcites (Table 2 and Fig. 5A). Although the stable carbon ($\delta^{13}C_{carb}$, VPDB) isotope values display a smaller difference between micrites and vein/vug-fill calcites in the 4GZ section, the latter does show slightly lower values, i.e., -3.4‰ to -4.0‰ *vs.* -3.9‰ to -4.8‰ (Fig. 5B). These stable isotope signatures, i.e., contrastingly different values between micrite and vein/vug-fill calcite, are similar to those reported in Wei et al. (2016) for the same rocks.

For carbonates from the 2GZ and 3GZ sections, there is also a difference in $\delta^{18}O_{carb}$ values between micrites and vein/vug-fill calcites, although much smaller compared to those in the 4GZ section, i.e., -8.6‰ to -12.0‰ (micrites) *vs.* -13.0‰ to -14.7‰ (vein/vug-fill calcites; Table 2 and Fig. 5A). The $\delta^{13}C_{carb}$ values of the 2GZ and 3GZ sections are generally similar to those in the 4GZ section (Fig. 5B).

4.4 Carbonate clumped isotope data

Distinct patterns of $T_{(\Delta 638)}$ temperatures are observed between micrite and vein/vug-fill calcite in different sections (Table 3 and Fig. 5C). As explained in section 3.5, outlier replicates were removed for the calculation of final $T_{(\Delta 638)}$. We compare the values obtained using this data processing method with (1) all replicates used for the calculation of final $T_{(\Delta 638)}$ and (2) the median values of all replicates (Supplementary Table S1 and Fig. S5). It is found that the reported values in Table 3 are similar to those obtained using the other two methods, with an average difference of 1.7 ± 1.8 °C and 1.6 ± 0.9 °C, respectively (Supplementary Table S1). More importantly, the differences between micrite and vein/vug-fill calcite remain consistent among all three data processing methods (Supplementary Fig. S5). This confirms the robustness of the observed $T_{(\Delta 638)}$ temperature variations as shown in Fig. 5C.

It is worth noting that the applied Δ_{638} – temperature equation (1) is a calcite-specific calibration equation (Yanay et al., 2022). However, XRD analysis indicates that the micrite samples are dominated by dolomite with limited calcite components (Table 1). Arguments still exist concerning whether different carbonate mineralogy, e.g., dolomite, calcite, and aragonite, has different clumped isotope temperature calibration equations. Some authors conclude there is no difference (Anderson et al., 2021; Bonifacie et al., 2017; Defliese et al., 2015; Petersen et al., 2019; Winkelstern et al., 2016), while others argue for mineral-specific calibration equations (Lu et al., 2022; Müller et al., 2019; Murray et al., 2016). In another more recent study, after reviewing all previous arguments and studies, it is suggested that there is no need for a dolomite-specific clumped isotope temperature calibration equation (Anderson et al., 2024).

According to Müller et al. (2019), the calculated formation temperatures for dolomite would be 3 to 16 °C colder by applying a calcite-specific equation than by applying a dolomite-specific equation. Following this argument, this would make the clumped isotope temperatures of the micrite samples of this study even higher than the values presented in Table 3. This would increase the clumped isotope temperature contrast (~7.4 °C on average) between the micrite and vein/vug-fill calcite in the 4GZ section. This larger temperature difference would not alter the following discussion of diagenesis. As such, we choose to apply equation (1) for all samples in this study as we do not yet have a dolomite-specific calibration equation for our Δ_{638} values.

In the 4GZ section, the $T_{(\Delta 638)}$ temperatures of the micrites are higher than plausible Earth's surface temperatures, ranging between 41.9 ± 4.3 °C and 50.3 ± 4.6 °C, while the vein/vug-fill calcites yield lower $T_{(\Delta 638)}$ temperatures ranging between 20.6 ± 3.5 °C and 30.8 ± 3.7 °C. In contrast, in the 2GZ and 3GZ sections, both micrites and vein/vug-fill calcites show similarly higher than Earth's surface $T_{(\Delta 638)}$ temperatures ranging between 41.1 ± 4.2 °C and 50.0 ± 4.4 °C. One micrite analysis of sample 3GZ153 returned a lower $T_{(\Delta 638)}$ temperature of 29.5 ± 3.8 °C, which is ~18 °C lower than another micrite analysis from the same sample but a different drilling spot (Table 3 and Fig. 5C).

We calculated the $\delta^{18}O_w$ values (VSMOW) of paleo-meteoric water from which the carbonate precipitated by using clumped isotope temperatures and $\delta^{18}O_{carb}$ values (Table 3 and Fig. 5D). For the 4GZ section, the calculated $\delta^{18}O_w$ values of vein/vug-fill calcites were generally lower (between -3.9 and -12.3‰, VSMOW) compared to corresponding micrite samples (between -0.3 and -2.7‰), but with large variations. In the 2GZ and 3GZ sections, the calculated $\delta^{18}O_w$ values of micrite and vein/vug-fill calcites are similar between -7.1 and -8.4‰. Notably, the one micrite analysis of sample 3GZ153, which has a lower $T_{(\Delta 638)}$ temperature of ~30 °C, also shows a lower calculated $\delta^{18}O_w$ value of -10.7‰ (Fig. 5D).

4.5 Results of solid-state reordering modeling

Our modeling indicates a burial temperature of at least ~170 °C is required to reorder the clumped isotope temperature of dolomite from ~30 °C to ~50 °C (Fig. 6A), while only ~142 °C is required to reorder the clumped isotope temperature of calcite from ~30 °C to ~50 °C (Fig. 6B). Additional model runs indicate that at a burial temperature of ~142 °C, the clumped isotope temperature of dolomite only slightly increases from ~30 °C to ~33.5°C (Fig. 6C), while at a burial temperature of ~170 °C, the clumped isotope temperature of calcite would have been increased from ~30 °C to 87.4°C (Fig. 6D). Reordering models assuming two other different burial and exhumation scenarios yielded similar results with negligible differences (Supplementary Table S2).

We acknowledge that the current reordering modeling parameters are ideal, and other carbonate properties, such as purity, crystallinity, presence of water or defects in the structure, and organic contents, could lead to the reordering of dolomite/calcite at lower temperatures, but to what extent we are unable to quantify.

4.6 Carbonate LA-ICP-MS U-Pb ages and trace element contents

Among the five carbonate U-Pb dating attempts (two micrite and three vein/vug-fill calcite samples), the two analyses on the vug-fill calcite of sample 4GZ96 yielded precise ages (Fig. 7). Two separate vug-fill calcite mounts of the same sample produced statistically indistinguishable ages of 3.0 ± 0.3 Ma (n=38; MSWD=4.0; 2σ) and 3.3 ± 0.1 Ma (n=88; MSWD=2.2; 2σ). In contrast, the other three samples (two micrite and one vein/vug-fill calcite samples) yield ages with large uncertainties. Micrite samples 4GZ11 and 4GZ18 yielded ages of -56 ± 130 Ma (n=45; MSWD=1.2; 2σ) and 76 ± 82 Ma (n=43; MSWD=0.3; 2σ), respectively (Supplementary Fig. S6), whereas no age was generated from another vein/vug-fill calcite sample 4GZ7V.

The two precisely dated vug-fill calcite samples have U content ranging between 1 and 10 ppm (mean 2.4±1.2 ppm and 3.8±1.9 ppm, respectively; Fig. 8), and the other vein/vug-fill calcite sample that does not yield an age has the lowest U content ranging between 0.05 and 1 ppm (mean 0.6±1.9 ppm). One of the micrite samples has U content ranging between 2 and 4 ppm (mean 2.5±0.4 ppm), while the other one has a much higher U content of 30–65 ppm (mean 58.1±6.3 ppm). The micrite and vein/vug-fill calcite samples also exhibit distinct Th abundance. Specifically, the two micrite samples exhibit much higher Th content of 31.8 ± 9.4 ppm and 3.3 ± 0.8 ppm, respectively, whereas all three vein/vug-fill calcite samples have Th content lower than 1 ppm (Fig. 8).

5. Discussion

5.1 Diagenetic stage of the 4GZ section vein/vug-fill calcite

We obtained new age and temperature information for the 4GZ section vein/vug-fill calcites, which can be used to determine the diagenetic stages to which they belong. Firstly, the $\delta^{18}O_{carb}$ (VPDB) values of vein/vug-fill calcites (-10.2‰ to -13.9‰) are lower than corresponding micrites (-4.5‰ to -6.4‰), suggesting formation at different stages (Table 2 and Fig. 5A). Secondly, the $T_{(\Delta 638)}$ temperatures from vein/vug-fill calcites are 21–31 °C, which are within the range of plausible Earth's surface $T_{(\Delta 638)}$ temperatures and thus argues against the possibility of mesogenesis (Fig. 2); but lower than those of corresponding micrite (42–50 °C) (Table 3 and Fig. 5C). Thirdly, the vein/vug-fill calcites of sample 4GZ96 crystallized at 3.0–3.3 Ma (Fig. 7), ~35 Myr after the early late Eocene deposition of the host micrite. Hence, the eogenesis origin of these vein/vug-fill calcites can be excluded (Fig. 2). Although no ages were obtained for the vein/vug-fill calcites of other samples, we infer that they also crystallized at 3.0–3.3 Ma given their similar stable isotope and clumped isotope values (Fig. 5). We conclude that the vein/vug-fill calcites of the 4GZ section, as well as those reported by Wei et al. (2016), were most likely formed during telogenesis after significant exhumation (refer to Fig. 2).

Thrusting in the frontal Himalaya is still ongoing (DeCelles et al., 1998; Yin, 2006), whereas the youngest evidence for thrust faulting in central Tibet is ~23–20 Ma, such as the shortening of the Nima Basin and near the Shiquanhe area (Fig. 1A) (Kapp et al., 2007; Kapp et al., 2003). East-west extension initiated in western central Tibet by ~10 Ma (Sundell et al., 2013; Woodruff Jr et al., 2013). Hence, crystallization of the ~3 Ma vein/vug-fill calcite was therefore coeval with upper crustal extensional tectonics in central Tibet.

5.2 Diagenetic history of the 4GZ section

While vein/vug-fill calcites of the 4GZ section formed during telogenesis, it is unclear whether the micrites in the same section also underwent diagenesis based on petrographic observations alone. However, the higher than plausible Earth's surface clumped isotope temperatures suggest either cryptic-recrystallization or solid-state reordering (Huntington and Lechler, 2015; Lacroix and Niemi, 2019).

XRD analysis revealed that samples 4GZ11, 18, and 79 are dominated by dolomite (92%–98%; Table 1), while samples 4GZ7 and 96 have lower percentages of dolomite at 44% and 56%, respectively. Petrographic observations and EPMA maps indicate that samples 4GZ7 and 96 contain pervasive vein/vug-fill calcite (Fig. 3D–E). The high calcite content of the bulk micrite of these two samples (Table 1) is likely due to contamination from vein/vug-fill calcites. Therefore, the micrite in samples 4GZ7 and 96 may be also dominated by dolomite.

Modern Earth's surface conditions make dolomite precipitation difficult, although direct dolomite precipitation from surface waters in the geologic past has been widely documented (Vasconcelos et al., 1995; Warren, 2000). Nonetheless, all the micrite samples of the 4GZ section have clumped isotope temperatures higher than plausible Earth's surface $T_{(\Delta 638)}$ temperatures (42–50 °C; Fig. 5C), indicating that these micrites have undergone diagenesis.

Two possible processes could explain the elevated $T_{(\Delta 638)}$ temperatures of the micrites. The first possibility is that the dolomite replaced primary calcite during shallow burial at a depth corresponding to 40–50 °C temperatures. If this is the case, the micrite $T_{(\Delta 638)}$ values record the temperature at the depth of dolomitization, and their stable isotopes reflect those of the fluid in which dolomitization occurred. Alternatively, the dolomite may have been primary, initially recording Earth's surface $T_{(\Delta 638)}$ temperatures, but later experienced solid-state reordering at deeper depth of ~170 °C burial temperatures (Fig. 6A). If this is the case, the 40–50 °C $T_{(\Delta 638)}$ temperatures are reordered temperatures although the $\delta^{18}O_{carb}$ values would not be altered by reordering and should retain their primary composition (Huntington and Lechler, 2015). However, the recalculated $\delta^{18}O_w$ values do not reflect surface waters as the $T_{(\Delta 638)}$ is reordered temperature.

We favor the first scenario of dolomitization during shallow burial for the following reasons. Firstly, for dolomite to be reordered to ~50 °C requires a minimal burial depth equivalent to temperatures of ~170 °C, under the assumed burial and exhumation history (Fig. 6A). However, field observations provide no evidence that these rocks were buried to such depth, but rather <2 km (i.e., <90 °C burial temperature, assuming surface temperature of 30 °C and a thermal gradient of 30 °C/km). This ~2 km burial depth inference is also likely a maximum based on two observations. First, our observations indicate that there is no evidence that younger strata were ever deposited on top of the 4GZ lacustrine rocks. Second, the 4GZ section is located on the hanging wall of a regional major thrust (GSBT, Fig. 1B) and all major thrust faults to the south are south-verging (Kapp and DeCelles, 2019). This suggests that there was no major structural burial of the 4GZ section after deposition. Under a burial temperature of 90 °C, dolomite minerals would not undergo reordering.

Secondly, the high U and Th content of the micrite (Fig. 8) suggests that the micrite most likely precipitated from fluids that are different from surface lake waters. The concentration of U in natural waters generally falls in the range of a few to tens of ppb (parts per billion) (Smedley and Kinniburgh, 2023; Waseem et al., 2015); and correspondingly, the U concentration in lacustrine carbonate is generally no more than 1 ppm (parts per million) due to element partitioning between water and carbonate (Elisha et al., 2021; Roberts et al., 2020). In rare circumstances, some lake waters can contain elevated U due to input from high U-bearing rocks in the catchment, or high U-bearing fluid transported from depth by fractures/faults. Although the partitioning of U has been extensively studied for calcite and aragonite (Smrzka et al., 2019), it has not yet been studied for dolomite. Nonetheless, the uptake of U in dolomite is unlikely to be higher than that in calcite, as it is much easier for U to replace Ca than Mg considering their atomic size differences (Rasbury et al., 2021). As a result, the difference in U content between vein/vug-fill calcite and micritic dolomite (Fig. 8) is not a result of different partitioning between calcite and dolomite but reflects the difference in U content in fluids. The contrast between the U and Th content in micrite compared to vein/vug-fill calcite indicates that the fluid from which the dolomite precipitated was most likely different from lake water, while the vein/vug-fill calcite was more likely precipitated from fluid that is compositionally similar to surface water, further agreeing with our interpretation that the vein/vug-fill calcite of the 4GZ section was formed during telogenesis near Earth's surface.

Based on the above discussion, we suggest the following diagenetic history to be most likely for the carbonate rocks in the 4GZ section. Initially, primary calcite was deposited in a lacustrine environment during the middle–late Eocene and initially recorded Earth's surface $T_{(\Delta 638)}$ temperatures and lake water's stable isotopic composition. Subsequently, during shallow burial to a depth equivalent to 40–50 °C, most of the calcite converted to dolomite in the presence of fluids different from surface waters (considering the high U and Th contents, Fig. 8). This process, however, did not visibly recrystallize the primary micritic texture. The carbonate rocks did not undergo any stable or clumped isotopic changes during further burial (no recrystallization and no solid-state reordering), probably due to the lack of fluids and shallow burial (<90 °C burial temperature). Finally, at ~3.0–3.3 Ma, when the 4GZ section was exhumed to near the Earth's surface, calcite-filled veins and vugs formed at near Earth's surface ambient temperatures of 20–30 °C.

5.3 Diagenesis of the 2GZ and 3GZ sections

The $T_{(\Delta 638)}$ temperatures of the two 3GZ micrite samples (41–48 °C) are within the temperature range of the 4GZ section micrites (Fig. 5C). However, the vein/vug-fill calcite of the

3GZ section and sparite of one fossil sample in the 2GZ section have similarly high $T_{(\Delta 638)}$ temperatures as the micrite samples, which is in contrast to the lower $T_{(\Delta 638)}$ temperatures of the vein/vug-fill calcite in the 4GZ section (20–30°C; Fig. 5C). Being situated at the opposite sides of a regional major thrust fault (GSBT, Fig. 1B), the temperature and isotopic differences between the 4GZ and 2GZ/3GZ sections might be linked to hydrological variations. For example, differing water sources and/or degrees of evaporation associated with the development of fold-thrust structures have been observed in the Pyrenees (Hoareau et al., 2021; Lacroix et al., 2014). However, we argue in the flowing the isotopic differences between different sections in the Gerze area are more likely the result of differing diagenetic conditions.

The two clumped isotope analyses of micrite in sample 3GZ153 yield two different $T_{(\Delta 638)}$ temperatures of 29.5 ± 3.8 °C and 47.7 ± 4.2 °C (Fig. 5C). There are two possible explanations for this $T_{(\Delta 638)}$ temperature difference: 1) the different $T_{(\Delta 638)}$ temperatures indicate multi-stage dolomitization under different ambient temperatures (burial depth); and 2) the higher $T_{(\Delta 638)}$ temperature records the temperature of dolomitization during shallow burial diagenesis, while the lower $T_{(\Delta 638)}$ temperature records the primary calcite formation temperature in surface lake water. We rule out the second interpretation because SEM energy dispersive X-ray spectroscopy (EDS) analysis indicates that the drilled powders for both clumped isotope analyses are dominantly dolomite (Supplementary file). If the first interpretation that we favor is correct, it would indicate that dolomitization is generally a long-term process during shallow burial. Previous studies have shown that early diagenetic dolomitization can be a continuous process from lake bottom/sea floor to intermediate burial depths (Machel, 2004). It is unlikely that the dolomite was primarily deposited in lake water and initially recorded lower temperatures (i.e., 30 °C), but later reordered to higher temperatures (i.e., ~50 °C), given the required maximum burial temperature of dolomite (i.e., 170 °C, Fig. 6A) and the calcite components in the same section would have been reordered to temperatures as high as 87°C (Fig. 6D) than measured (~50 °C) if buried to a depth corresponding to ~170 °C temperatures.

Assuming that the high $T_{(\Delta 638)}$ temperatures of the 2GZ/3GZ micrites can be reasonably explained as shallow burial dolomitization, the similarly high $T_{(\Delta 638)}$ temperatures of the vein/vug-fill calcite in the same sections may have two different explanations: 1) the vein/vug-fill calcite was formed during early diagenesis under similar conditions as the dolomitization, i.e., similar depth/temperature, but probably in a later time; and 2) the vein/vug-fill calcite was formed at lower near Earth's surface temperatures, but later experienced solid-state reordering to record higher clumped isotope temperatures. Solid state reordering modeling indicates that this can be achieved if the 2GZ and 3GZ sections were buried to a depth corresponding to ~142 °C temperatures (Fig. 6B). The 2GZ/3GZ sections are located in the footwall of a regional major north-verging thrust fault (GSBT, Fig. 1B). Consequently, these two sections could have been structurally buried by thrusting as well as by emplacement of overlying volcanic rocks (Tv, Fig. 1B). Under ~142°C burial temperature, the dolomitic micrite would only be slightly reordered (~3.5°C increase; Fig. 6C). However, we favor the first explanation, as if the vein/vug-fill calcites were formed at lower near Earth's surface temperatures (~30 °C), aka, earlier than dolomitization at higher burial temperatures (~50 °C), it would be difficult to explain why these vein/vug-fill calcites didn't experience dolomitization as the micrites.

5.4 Implications for paleoelevation estimates

The interpreted diagenetic history of the 4GZ section provides new insights into previous estimates of paleoelevations of the Gerze area. Ingalls et al. (2020) interpreted the vein/vug-fill calcite of the 4GZ section to be formed during eogenesis and thus preserved primary surface water isotopic values. This inference led to the conclusion of the attainment of high elevations during the middle–late Eocene, based on the low $\delta^{18}O_{carb}$ values of the vein/vug-fill calcites. However, our findings suggest a telogenetic origin for the vein/vug-fill calcites in the 4GZ section, and that they crystallized and recorded the stable isotopic composition of surface waters at 3.0–3.3 Ma.

Wei et al. (2016) inferred that the 4GZ section was at or near sea-level elevations during the middle–late Eocene. In addition to the discovery of six marine foraminifera shells possibly transported by storm surges, the main evidence to support their low-elevation conclusion is the interpretation of an open-lake condition with very positive $\delta^{18}O_w$ values (-2.8 ± 1.1‰, assuming carbonate precipitation temperatures of 25 ± 10 °C). The open lake condition is critical for this interpretation, as these more positive $\delta^{18}O_w$ values could also be a result of evaporative enrichment in closed lakes of any elevation. Two observations led Wei et al. (2016) to suggest an open-lake condition: 1) a poor correlation between the $\delta^{18}O_{carb}$ and $\delta^{13}C_{carb}$ values; and 2) a relatively narrow range of the $\delta\ ^{18}O_{carb}$ values (e.g., Horton et al., 2016; Talbot, 1990). Our interpretation of shallow burial diagenesis (dolomitization) of the micrites provides an alternative explanation for these two observations. As the inferred dolomitization occurred during shallow burial (<1 km depth), the stable oxygen isotopes of ambient fluid most likely reflect groundwater composition that is more homogeneous compared to surface waters, i.e., more isotopically buffered. Thus, the lack of correlation between the $\delta^{18}O_{carb}$ and $\delta^{13}C_{carb}$ values might be a result of diagenesis in groundwater that is more homogeneous compared to lake water, but not open-lake conditions. On the other hand, since the entire section underwent dolomitization under similar conditions, the $\delta^{18}O_{carb}$ values of all the micrites would be controlled by the diagenetic fluid (homogenized groundwater) and thus would lack large variations.

While our new findings raise questions about the evidence cited by Wei et al. (2016) in support of their low-elevation interpretation, it remains possible that the 4GZ section during the middle–late Eocene was an open lake at low elevations. The calculated $\delta^{18}O_w$ values of the relatively shallowly buried fluids in which dolomitization occurred show relatively positive values of -0.3 to -2.7‰ (Fig. 5D and Table 2). If the fluids originated from surface lake water (i.e., similar stable oxygen isotope values but different trace element content), then the positive $\delta^{18}O_w$ values indicate either low paleoelevations or evaporative enrichment of lake water during the middle–late Eocene.

Triple oxygen isotope analyses could be used to test these scenarios and assess the degree of evaporation and help distinguish between open-lake versus closed-lake scenarios (Aron et al., 2020; Passey and Ji, 2019). However, even if triple oxygen isotope studies indicate strong evaporation, this would not necessarily rule out a low paleoelevation scenario for the lake floor, since the more negative primary lake waters in a closed lake scenario could have come from a high-elevation catchment, while the lake remained at low elevation. Given that the 4GZ section micrites have undergone shallow burial diagenetic dolomitization, it may be challenging to determine the paleoelevation of the middle–late Eocene lake basin based on the analysis of 4GZ section rocks alone. The stable and clumped isotope analysis of paleosol carbonate may help solve this problem. However, unfortunately, paleosol carbonates have not been found in this section.

In the 2GZ/3GZ sections, it is possible that the fluid in which the diagenetic dolomitization occurred originated from surface water. If this was the case, then the most negative $\delta^{18}O_w$ values (VSMOW) of -10.7% (Table 3) could be used to estimate a paleoelevation of ~3.2 km using the modified stable isotope-based paleoaltimetry method outlined in Li, L. et al. (2022). However, this paleoelevation estimate would be a maximum for the basin floor, as the water is an average of the catchment that would include the Gangdese mountains to the south and/or the Qiangtang mountains to the north (Song et al., 2023). This moderately high paleoelevation in the catchment does not contradict the inference of an Eocene low-elevation valley in central Tibet, as suggested by Wei et al. (2016) and several other studies in the Lunpola Basin (Li, L. et al., 2022; Su et al., 2019; Wu et al., 2017). We refer readers to Li, L. et al. (2022) for a detailed assessment of existing paleoelevation studies in central Tibet and associated arguments concerning the Eocene central Tibet valley.

Reliable paleoelevation estimates might be not yet available for the middle–late Eocene in the Gerze area. The calculated $\delta^{18}O_w$ values (VSMOW) of the paleo-meteoric water from which the 4GZ section telogenetic vein/vug-fill calcite precipitated were as low as -12.3‰ (Fig. 5D and Table 3). This value is similar to those of modern precipitation and surface waters in the Gerze area, which are between -11 and -13‰ (DeCelles et al., 2007; Li and Garzione, 2017), indicating that the 4GZ section was most likely at its present elevation at 3.0–3.3 Ma.

6. Conclusion

Carbonate rocks are prone to diagenesis, and it is important to identify the stages of diagenesis, e.g., eogenesis, mesogenesis, and telogenesis, with implications for the interpretation of paleoclimate and paleoelevation. We combined stable isotopes, clumped isotope temperatures, and carbonate formation ages to determine carbonate diagenetic stages. This same toolset and criteria (Fig. 2) can be used in other carbonate diagenesis studies in general.

We determined that the vein/vug-fill calcites in the middle–late Eocene lacustrine carbonate samples in the southeastern Gerze area 4GZ section exhibit $\delta^{18}O_{carb}$ values between -10 and -14‰, Earth's surface $T_{(\Delta 638)}$ temperatures (20–30 °C), and 3.0–3.3 Ma crystallization ages. Collectively, these results indicate a telogenetic origin for these vein/vug-fill calcites. Our findings also reveal that the lacustrine micrites have higher than Earth's surface $T_{(\Delta 638)}$ temperatures (40–50 °C), are dominantly dolomite in composition, and display U and Th concentrations that are higher than typical lake waters. Collectively, these results suggest that the micrite experienced dolomitization during shallow burial to temperatures of 40–50 °C.

Our results have important implications for previous paleoelevation interpretations of the southeastern Gerze area (4GZ section). We argue that the low $\delta^{18}O_{carb}$ values of the vein/vug-fill calcites do not represent high elevations during the middle–late Eocene (Ingalls et al., 2020), but rather indicate high elevations during east-west upper-crustal extension at 3.0–3.3 Ma. We also explain why previous evidence used to argue for an open-lake condition to support a low-elevation interpretation in the Gerze region might be compromised by shallow burial diagenesis. Although the low-elevation inference of Wei et al. (2016) is consistent with the calculated positive shallow groundwater compositions, existing evidence is inconclusive as to the paleoelevation of the basin floor of the Gerze area during the middle–late Eocene.

Acknowledgements

We would like to thank William Defliese for discussion of solid-state reordering modeling, Zhennan Wang for help with clumped isotope analysis, Andrei Astashkin for XRD data collection, and Kenneth Domanik for help with EPMA analysis. We thank Stefano Bernasconi for editorial handling, Brice Lacroix and two other anonymous reviewers for comments and suggestions that greatly helped clarify the content of this study. This work was supported by NSF grants EAR-2048656 and OISE-1545859.

Data Availability

All data associated with this paper (Data S1: clumped isotope data of new samples; Data S2: clumped isotope data of standards; and Data S3: carbonate LA-ICPMS U-Pb data) are available through Zenodo at: https://doi.org/10.5281/zenodo.10196493.

Appendix A. Supplementary material

The supplementary file includes two tables: Table S1, comparisons of clumped isotope temperatures using different data processing methods; Table S2, Summary of solid-state reordering modeling results. Six figures: Fig. S1. Stratigraphic columns of measured sedimentary sections in the Gerze area. Fig. S2–S4 show EPMA maps of all measured elements (Ca, Mg, Si, Fe, Mn, Sr, Cr, and Ba) for sample 4GZ7_coarse scale (Fig. S2), 4GZ96_coarse scale (Fig. S3), and 4GZ96_fine scale (Fig. S4); Fig. S5 shows the comparison of clumped isotope temperatures between three different data processing methods; Fig. S6 shows the Tera-Wasserburg plots of the carbonate U-Pb data of 4GZ11 and 4GZ18. Also included are the EDS analysis results for sample 3GZ153. The supplementary file can be found online at xxx.

References

Anderson, N., Bonifacie, M., Jost, A., Siebert, J., Bontognali, T., Horita, J., Müller, I., Bernasconi, S., Bergmann, K., 2024. Re-assessing the need for apatite-and dolomite-specific calibrations of the carbonate clumped isotope thermometer. Geochemi., Geophy., Geosy. 25(1), e2023GC011049.

Anderson, N.T., Kelson, J.R., Kele, S., Daëron, M., Bonifacie, M., Horita, J., Mackey, T.J., John, C.M., Kluge, T., Petschnig, P., 2021. A unified clumped isotope thermometer calibration (0.5–1,100 c) using carbonate-based standardization. Geophys. Res. Lett. 48(7), e2020GL092069.

Armenteros, I., 2010. Diagenesis of carbonates in continental settings, in: Alonso-Zarza, A.M., Tanner, L.H. (Eds.), Carbonates in continental settings. Elsevier, pp. 61-151.

Aron, P.G., Levin, N.E., Beverly, E.J., Huth, T.E., Passey, B.H., Pelletier, E.M., Poulsen, C.J., Winkelstern, I.Z., Yarian, D.A., 2021. Triple oxygen isotopes in the water cycle. Chem. Geol. 565, 120026.

Bernasconi, S.M., Daëron, M., Bergmann, K.D., Bonifacie, M., Meckler, A.N., Affek, H.P., Anderson, N., Bajnai, D., Barkan, E., Beverly, E., 2021. Intercarb: A community effort to improve interlaboratory standardization of the carbonate clumped isotope thermometer using carbonate standards. Geochemi., Geophy., Geosy. 22(5), e2020GC009588.

Bonifacie, M., Calmels, D., Eiler, J.M., Horita, J., Chaduteau, C., Vasconcelos, C., Agrinier, P., Katz, A., Passey, B.H., Ferry, J.M., 2017. Calibration of the dolomite clumped isotope thermometer from 25 to 350° c, and implications for a universal calibration for all (ca, mg, fe) co3 carbonates. Geochim. Cosmochim. Acta 200, 255-279.

Cai, C., Huang, D., Wu, F., Zhao, M., Wang, N., 2019. Tertiary water striders (hemiptera, gerromorpha, gerridae) from the central Tibetan Plateau and their palaeobiogeographic implications. J. Asian Earth Sci. 175, 121-127.

Chamberlain, C.P., Poage, M., 2000. Reconstructing the paleotopography of mountain belts from the isotopic composition of authigenic minerals. Geology 28(2), 115-118.

Choquette, P.W., Pray, L.C., 1970. Geologic nomenclature and classification of porosity in sedimentary carbonates. AAPG Bull. 54(2), 207-250.

Cong, F., Tian, J., Hao, F., Licht, A., Liu, Y., Cao, Z., Eiler, J.M., 2021. A thermal pulse induced by a permian mantle plume in the tarim basin, northwest china: Constraints from clumped isotope thermometry and in situ calcite u-pb dating. J. Geophys. Res. Solid Earth 126(4), e2020JB020636.

Daëron, M., 2021. Full propagation of analytical uncertainties in δ47 measurements. Geochemi., Geophy., Geosy. 22(5), e2020GC009592.

DeCelles, P., Gehrels, G., Quade, J., Ojha, T., Kapp, P., Upreti, B., 1998. Neogene foreland basin deposits, erosional unroofing, and the kinematic history of the Himalayan fold-thrust belt, western Nepal. Geol. Soc. Am. Bull. 110(1), 2-21.

DeCelles, P.G., Quade, J., Kapp, P., Fan, M., Dettman, D.L., Ding, L., 2007. High and dry in central Tibet during the late Oligocene. Earth Planet. Sci. Lett. 253(3-4), 389-401.

Defliese, W.F., Hren, M.T., Lohmann, K.C., 2015. Compositional and temperature effects of phosphoric acid fractionation on δ47 analysis and implications for discrepant calibrations. Chem. Geol. 396, 51-60.

Dennis, K.J., Affek, H.P., Passey, B.H., Schrag, D.P., Eiler, J.M., 2011. Defining an absolute reference frame for 'clumped' isotope studies of CO2. Geochim. Cosmochim. Acta 75(22), 7117-7131.

Ding, L., Kapp, P., Cai, F., Garzione, C.N., Xiong, Z., Wang, H., Wang, C., 2022. Timing and mechanisms of Tibetan Plateau uplift. Nat. Rev. Earth Environ. 3, 652-667.

Eiler, J.M., Schauble, E., 2004. 18O13C16O in Earth's atmosphere. Geochim. Cosmochim. Acta 68(23), 4767-4777.

Elisha, B., Nuriel, P., Kylander-Clark, A., Weinberger, R., 2021. Towards in situ u–pb dating of dolomite. Geochronology 3(1), 337-349.

Garzione, C.N., Dettman, D.L., Quade, J., DeCelles, P.G., Butler, R.F., 2000. High times on the tibetan plateau: Paleoelevation of the thakkhola graben, nepal. Geology 28(4), 339-342.

Garzione, C.N., McQuarrie, N., Perez, N.D., Ehlers, T.A., Beck, S.L., Kar, N., Eichelberger, N., Chapman, A.D., Ward, K.M., Ducea, M.N., Lease, R.O., Poulsen, C.J., Wagner, L.S., Saylor, J.E., Zandt, G., Horton, B.K., 2017. The tectonic evolution of the central Andean plateau and geodynamic implications for the growth of plateaus. Annu. Rev. Earth Planet. Sci. 45, 529-559.

Gasparrini, M., Morad, D., Mangenot, X., Bonifacie, M., Morad, S., Nader, F., Gerdes, A., 2023. Dolomite recrystallization revealed by Δ47/u-pb thermochronometry in the upper jurassic arab formation, united arab emirates. Geology 51(5), 471-475.

Ghosh, P., Adkins, J., Affek, H., Balta, B., Guo, W., Schauble, E.A., Schrag, D., Eiler, J.M., 2006. 13C–18O bonds in carbonate minerals: A new kind of paleothermometer. Geochim. Cosmochim. Acta 70(6), 1439-1456.

Hemingway, J.D., Henkes, G.A., 2021a. A disordered kinetic model for clumped isotope bond reordering in carbonates. Earth Planet. Sci. Lett. 566, 116962.

Hemingway, J.D., Henkes, G.A., 2021b. Corrigendum to “a disordered kinetic model for clumped isotope bond reordering in carbonates” [earth planet. Sci. Lett. 566 (2021) 116962]. Earth and Planetary Science Letters 575, 117191.

Henkes, G.A., Passey, B.H., Grossman, E.L., Shenton, B.J., Pérez-Huerta, A., Yancey, T.E., 2014. Temperature limits for preservation of primary calcite clumped isotope paleotemperatures. Geochim. Cosmochim. Acta 139(5), 362-382.

Hill, C.A., Polyak, V.J., Asmerom, Y., Provencio, P.P., 2016. Constraints on a late Cretaceous uplift, denudation, and incision of the Grand Canyon region, southwestern Colorado Plateau, USA, from U-Pb dating of lacustrine limestone. Tectonics 35(4), 896-906.

Hoareau, G., Crognier, N., Lacroix, B., Aubourg, C., Roberts, N.M., Niemi, N., Branellec, M., Beaudoin, N., Ruiz, I.S., 2021. Combination of Δ47 and u-pb dating in tectonic calcite veins unravel the last pulses related to the pyrenean shortening (spain). Earth Planet. Sci. Lett. 553, 116636.

Horton, T.W., Defliese, W.F., Tripati, A.K., Oze, C., 2016. Evaporation induced 18O and 13C enrichment in lake systems: A global perspective on hydrologic balance effects. Quat. Sci. Rev. 131, 365-379.

Hu, X., Ma, A., Xue, W., Garzanti, E., Cao, Y., Li, S.-M., Sun, G., Lai, W., 2022. Exploring a lost ocean in the Tibetan Plateau: Birth, growth, and demise of the Bangong-Nujiang Ocean. Earth-Sci. Rev. 229, 104031.

Huntington, K.W., Lechler, A.R., 2015. Carbonate clumped isotope thermometry in continental tectonics. Tectonophysics 647–648(0), 1-20.

Ingalls, M., 2019. Reconstructing carbonate alteration histories in orogenic sedimentary basins: Xigaze forearc, southern Tibet. Geochim. Cosmochim. Acta 251, 284-300.

Ingalls, M., Rowley, D.B., Currie, B.S., Colman, A.S., 2020. Reconsidering the uplift history and peneplanation of the northern Lhasa terrane, Tibet. Am. J. Sci. 320(6), 479-532.

Kapp, P., DeCelles, P.G., 2019. Mesozoic–cenozoic geological evolution of the himalayan-tibetan orogen and working tectonic hypotheses. Am. J. Sci. 319(3), 159-254.

Kapp, P., DeCelles, P.G., Gehrels, G.E., Heizler, M., Ding, L., 2007. Geological records of the Lhasa-Qiangtang and Indo-Asian collisions in the Nima area of central Tibet. Geol. Soc. Am. Bull. 119(7-8), 917-933.

Kapp, P., Murphy, M.A., Yin, A., Harrison, T.M., Ding, L., Guo, J., 2003. Mesozoic and cenozoic tectonic evolution of the shiquanhe area of western tibet. Tectonics 22(4), 2001TC001332.

Kapp, P., Yin, A., Harrison, T.M., Ding, L., 2005. Cretaceous-Tertiary shortening, basin development, and volcanism in central Tibet. Geol. Soc. Am. Bull. 117(7-8), 865-878.

Kim, S.T., O'Neil, J.R., 1997. Equilibrium and nonequilibrium oxygen isotope effects in synthetic carbonates. Geochim. Cosmochim. Acta 61(16), 3461-3475.

Kylander-Clark, A.R.C., 2020. Expanding the limits of laser-ablation U-Pb calcite geochronology. Geochronology 2(2), 343-354.

Lacroix, B., Buatier, M., Labaume, P., Travé, A., Dubois, M., Charpentier, D., Ventalon, S., Convert-Gaubier, D., 2011. Microtectonic and geochemical characterization of thrusting in a foreland basin: Example of the south-Pyrenean orogenic wedge (Spain). J. Struct. Geol. 33(9), 1359-1377.

Lacroix, B., Niemi, N.A., 2019. Investigating the effect of burial histories on the clumped isotope thermometer: An example from the Green River and Washakie Basins, Wyoming. Geochim. Cosmochim. Acta 247, 40-58.

Lacroix, B., Travé, A., Buatier, M., Labaume, P., Vennemann, T., Dubois, M., 2014. Syntectonic fluid-flow along thrust faults: Example of the south-pyrenean fold-and-thrust belt. Mar. Pet. Geol. 49, 84-98.

Li, C., Zhao, Z., Lu, H., Li, H., 2022. Late Mesozoic-Cenozoic multistage exhumation of the central Bangong-Nujiang suture, central Tibet. Tectonophysics 827, 229268.

Li, L., Garzione, C.N., 2017. Spatial distribution and controlling factors of stable isotopes in meteoric waters on the Tibetan Plateau: Implications for paleoelevation reconstruction. Earth Planet. Sci. Lett. 460, 302-314.

Li, L., Garzione, C.N., Fan, M.J., Li, X.W., Li, X.Z., 2019. Jurassic sedimentation in the south-central Qiangtang terrane reveals successive terrane collisions in central Tibet. Geosphere 15(2), 433-449.

Li, L., Lu, H., Garzione, C.N., Fan, M.J., 2022. Cenozoic paleoelevation history of the Lunpola Basin in central Tibet: New evidence from volcanic glass hydrogen isotopes and a critical review. Earth-Sci. Rev. 231, 104068.

Li, Q., Parrish, R.R., Horstwood, M.S.A., McArthur, J.M., 2014. U–pb dating of cements in mesozoic ammonites. Chem. Geol. 376, 76-83.

Li, S., Yin, C., Guilmette, C., Ding, L., Zhang, J., 2019. Birth and demise of the Bangong-Nujiang Tethyan Ocean: A review from the Gerze area of central Tibet. Earth-Sci. Rev. 198, 102907.

Lloyd, M.K., Ryb, U., Eiler, J.M., 2018. Experimental calibration of clumped isotope reordering in dolomite. Geochim. Cosmochim. Acta 242, 1-20.

Lu, C., Murray, S., Koeshidayatullah, A., Swart, P.K., 2022. Clumped isotope acid fractionation factors for dolomite and calcite revisited: Should we care? Chem. Geol. 588, 120637.

Machel, H.G., 2004. Concepts and models of dolomitization: A critical reappraisal. Geol. Soc. London, Spec. Publ. 235(1), 7-63.

Mangenot, X., Gasparrini, M., Gerdes, A., Bonifacie, M., Rouchon, V., 2018. An emerging thermochronometer for carbonate-bearing rocks: Δ47/(u-pb). Geology 46(12), 1067-1070.

Müller, I.A., Rodriguez-Blanco, J.D., Storck, J.-C., do Nascimento, G.S., Bontognali, T.R., Vasconcelos, C., Benning, L.G., Bernasconi, S.M., 2019. Calibration of the oxygen and clumped isotope thermometers for (proto-) dolomite based on synthetic and natural carbonates. Chem. Geol. 525, 1-17.

Murray, S.T., Arienzo, M.M., Swart, P.K., 2016. Determining the δ47 acid fractionation in dolomites. Geochim. Cosmochim. Acta 174, 42-53.

Nenna, F., Aydin, A., 2011. The formation and growth of pressure solution seams in clastic rocks: A field and analytical study. J. Struct. Geol. 33(4), 633-643.

Nuriel, P., Wotzlaw, J.F., Ovtcharova, M., Vaks, A., Stremtan, C., Šala, M., Roberts, N.M.W., Kylander-Clark, A.R.C., 2021. The use of ash-15 flowstone as a matrix-matched reference material for laser-ablation U-Pb geochronology of calcite. Geochronology 3(1), 35-47.

Passey, B.H., Henkes, G.A., 2012. Carbonate clumped isotope bond reordering and geospeedometry. Earth Planet. Sci. Lett. 351, 223-236.

Passey, B.H., Ji, H., 2019. Triple oxygen isotope signatures of evaporation in lake waters and carbonates: A case study from the western United States. Earth Planet. Sci. Lett. 518, 1-12.

Paton, C., Hellstrom, J., Paul, B., Woodhead, J., Hergt, J., 2011. Iolite: Freeware for the visualisation and processing of mass spectrometric data. J. Anal. At. Spectrom. 26(12), 2508-2518.

Petersen, S.V., Defliese, W.F., Saenger, C., Daëron, M., Huntington, K.W., John, C.M., Kelson, J.R., Bernasconi, S.M., Colman, A.S., Kluge, T., 2019. Effects of improved 17o correction on interlaboratory agreement in clumped isotope calibrations, estimates of mineral‐specific offsets, and temperature dependence of acid digestion fractionation. Geochem. Geophys. Geosyst. 20(7), 3495-3519.

Polissar, P.J., Freeman, K.H., Rowley, D.B., McInerney, F.A., Currie, B.S., 2009. Paleoaltimetry of the Tibetan Plateau from D/H ratios of lipid biomarkers. Earth Planet. Sci. Lett. 287(1-2), 64-76.

Quade, J., Dettinger, M., Carrapa, B., DeCelles, P., Murray, K., Huntington, K., Cartwright, A., Canavan, R., Gehrels, G., Clementz, M., 2015. The growth of the central Andes, 22S–26S. Geol. Soc. Am. Mem. 12, 277-308.

Quade, J., Leary, R., Dettinger, M.P., Orme, D., Krupa, A., DeCelles, P.G., Kano, A., Kato, H., Waldrip, R., Huang, W., 2020. Resetting southern Tibet: The serious challenge of obtaining primary records of paleoaltimetry. Global Planet. Change 191, 103194.

Rasbury, E.T., Present, T.M., Northrup, P., Tappero, R.V., Lanzirotti, A., Cole, J.M., Wooton, K.M., Hatton, K., 2021. Tools for uranium characterization in carbonate samples: Case studies of natural u–pb geochronology reference materials. Geochronology 3(1), 103-122.

Roberts, N.M., Holdsworth, R.E., 2022. Timescales of faulting through calcite geochronology: A review. J. Struct. Geol. 158, 104578.

Roberts, N.M.W., Drost, K., Horstwood, M.S.A., Condon, D.J., Chew, D., Drake, H., Milodowski, A.E., McLean, N.M., Smye, A.J., Walker, R.J., Haslam, R., Hodson, K., Imber, J., Beaudoin, N., Lee, J.K., 2020. Laser ablation inductively coupled plasma mass spectrometry (LA-ICP-MS) U-Pb carbonate geochronology: Strategies, progress, and limitations. Geochronology 2(1), 33-61.

Roberts, N.M.W., Rasbury, E.T., Parrish, R.R., Smith, C.J., Horstwood, M.S.A., Condon, D.J., 2017. A calcite reference material for LA-ICP-MS U-Pb geochronology. Geochem. Geophys. Geosyst. 18(7), 2807-2814.

Rowley, D.B., Currie, B.S., 2006. Palaeo-altimetry of the late Eocene to Miocene Lunpola Basin, central Tibet. Nature 439(7077), 677-681.

Rowley, D.B., Garzione, C.N., 2007. Stable isotope-based paleoaltimetry. Annu. Rev. Earth Planet. Sci. 35, 463-508.

Rowley, D.B., Pierrehumbert, R.T., Currie, B.S., 2001. A new approach to stable isotope-based paleoaltimetry: Implications for paleoaltimetry and paleohypsometry of the high himalaya since the late miocene. Earth Planet. Sci. Lett. 188(1-2), 253-268.

Shenton, B.J., Grossman, E.L., Passey, B.H., Henkes, G.A., Becker, T.P., Laya, J.C., Perez-Huerta, A., Becker, S.P., Lawson, M., 2015. Clumped isotope thermometry in deeply buried sedimentary carbonates: The effects of bond reordering and recrystallization. Geol. Soc. Am. Bull. B31169. 31161.

Smedley, P., Kinniburgh, D., 2023. Uranium in natural waters and the environment: Distribution, speciation and impact. J. Appl. Geochem. 148, 105534.

Smrzka, D., Zwicker, J., Bach, W., Feng, D., Himmler, T., Chen, D., Peckmann, J., 2019. The behavior of trace elements in seawater, sedimentary pore water, and their incorporation into carbonate minerals: A review. Facies 65, 1-47.

Song, B., Zhang, K., Wei, Y., Jiang, G., Yang, T., Algeo, T.J., Wang, J., Han, F., 2023. Paleogene sediment provenance in the gaize basin: Implications for early cenozoic paleogeography of central tibet. Palaeogeogr. Palaeoclimatol. Palaeoecol. 632, 111860.

Stolper, D.A., Eiler, J.M., 2015. The kinetics of solid-state isotope-exchange reactions for clumped isotopes: A study of inorganic calcites and apatites from natural and experimental samples. Am. J. Sci. 315(5), 363-411.

Su, T., Farnsworth, A., Spicer, R.A., Huang, J., Wu, F.X., Liu, J., Li, S.F., Xing, Y.W., Huang, Y.J., Deng, W.Y.D., 2019. No high Tibetan plateau until the Neogene. Sci. Adv. 5, eaav2189.

Su, T., Spicer, R.A., Wu, F.-X., Farnsworth, A., Huang, J., Del Rio, C., Deng, T., Ding, L., Huang, Y.-J., Hughes, A., 2020. A middle Eocene lowland humid subtropical "Shangri-La" ecosystem in central Tibet. Proc. Natl. Acad. Sci. 117(52), 32989-32995.

Sundell, K.E., Taylor, M.H., Styron, R.H., Stockli, D.F., Kapp, P., Hager, C., Liu, D.L., Ding, L., 2013. Evidence for constriction and pliocene acceleration of east-west extension in the north lunggar rift region of west central tibet. Tectonics 32, 1-26.

Swart, P.K., 2015. The geochemistry of carbonate diagenesis: The past, present and future. Sedimentology 62, 1233-1304.

Talbot, M.R., 1990. A review of the palaeohydrological interpretation of carbon and oxygen isotopic ratios in primary lacustrine carbonates. Chem. Geol.: Iso. Geosci. Sect. 80(4), 261-279.

Tera, F., Wasserburg, G., 1972. U-Th-Pb systematics in three apollo 14 basalts and the problem of initial pb in lunar rocks. Earth Planet. Sci. Lett. 14(3), 281-304.

Tong, K., Li, Z., Zhu, L., Xu, G., Zhang, Y., Kamp, P.J., Tao, G., Yang, W., Li, J., Wang, Z., 2022. Thermochronology constraints on the cretaceous-cenozoic thermo-tectonic evolution in the gaize region, central-western Tibetan Plateau: Implications for the westward extension of the proto-Tibetan Plateau. J. Asian Earth Sci. 240, 105419.

Vasconcelos, C., McKenzie, J.A., Bernasconi, S., Grujic, D., Tiens, A.J., 1995. Microbial mediation as a possible mechanism for natural dolomite formation at low temperatures. Nature 377(6546), 220-222.

Vasconcelos, C., McKenzie, J.A., Warthmann, R., Bernasconi, S.M., 2005. Calibration of the δ18O paleothermometer for dolomite precipitated in microbial cultures and natural environments. Geology 33(4), 317-320.

Wang, Z., Nelson, D.D., Dettman, D.L., McManus, J.B., Quade, J., Huntington, K.W., Schauer, A.J., Sakai, S., 2020. Rapid and precise analysis of carbon dioxide clumped isotopic composition by tunable infrared laser differential spectroscopy. Anal. Chem. 92(2), 2034-2042.

Warren, J., 2000. Dolomite: Occurrence, evolution and economically important associations. Earth-Sci. Rev. 52(1-3), 1-81.

Waseem, A., Ullah, H., Rauf, M.K., Ahmad, I., 2015. Distribution of natural uranium in surface and groundwater resources: A review. Crit. Rev. Environ. Sci. Technol. 45(22), 2391-2423.

Wei, Y., Zhang, K., Garzione, C.N., Xu, Y., Song, B., Ji, J., 2016. Low palaeoelevation of the northern lhasa terrane during late eocene: Fossil foraminifera and stable isotope evidence from the Gerze Basin. Sci. Rep. 6, 27508.

Winkelstern, I.Z., Kaczmarek, S.E., Lohmann, K.C., Humphrey, J.D., 2016. Calibration of dolomite clumped isotope thermometry. Chem. Geol. 443, 32-38.

Woodruff Jr, W.H., Horton, B.K., Kapp, P., Stockli, D.F., 2013. Late cenozoic evolution of the lunggar extensional basin, tibet: Implications for basin growth and exhumation in hinterland plateaus. Geol. Soc. Am. Bull. 125(3-4), 343-358.

Wu, F., Miao, D., Chang, M.-m., Shi, G., Wang, N., 2017. Fossil climbing perch and associated plant megafossils indicate a warm and wet central Tibet during the late oligocene. Sci. Rep. 7: 878, DOI:10.1038/s41598-017-00928-9.

Xiong, Z.Y., Liu, X.H., Ding, L., Farnsworth, A., Spicer, R.A., Xu, Q., Valdes, P., He, S.L., Zeng, D., Wang, C., Li, Z.Y., Guo, X.D., Su, T., Zhao, C.Y., Wang, H.Q., Yue, Y.H., 2022. The rise and demise of the Paleogene central Tibetan valley. Sci. Adv. 8(6), eabj0944.

Yanay, N., Wang, Z., Dettman, D.L., Quade, J., Huntington, K., Schauer, A., Nelson, D.D., McManus, B., Thirumalai, K., Sakai, S., 2022. Rapid and precise measurement of carbonate clumped isotopes using laser spectroscopy. Sci. Adv. 8(43), eabq0611.

Yin, A., 2006. Cenozoic tectonic evolution of the himalayan orogen as constrained by along-strike variation of structural geometry, exhumation history, and foreland sedimentation. Earth-Sci. Rev. 76(1), 1-131.

Yin, A., Harrison, T.M., 2000. Geologic evolution of the Himalayan-Tibetan orogen. Annu. Rev. Earth Planet. Sci. 28(1), 211-280.

Zhang, Y.L., Shen, Y.X., Wu, Z.H., Zhao, Z., 2018. Zircon U-Pb ages of magmatic rocks from meisu formation in gerze area in Tibet and its geological significance. J. Geomech. 24(1), 128-136.

Table 1. X-ray diffraction (XRD) results.

Sample ID	Dolomite (wt%)	Calcite (wt%)	Quartz (wt%)	Others (wt%)	Dolomite+Calcite (wt%)	Dolomite ratio* (%)
4GZ7	41	52[#]	6	1	93	44
4GZ11	87	8	2	3	95	92
4GZ18	88	2	8	2	90	98
4GZ79	77	2	15	6	79	97
4GZ96	53	42[#]	4	1	95	56
2GZ58	0	84	2	14	84	0
3GZ153	47	23	20	10	70	67
3GZ173	42	7	37	14	49	86

Note: wt%, weight percentage.

*dolomite ratio is defined as dolomite/(dolomite+calcite).

[#] The high calcite content of these two samples is due to the pervasive distribution of vein/vug-fill calcite (e.g., Fig. 3D–E), which is unavoidable during the powdering process for XRD analysis.

Table 2. Summary of carbonate stable isotope data*.

Sample name	$\delta^{13}C_{carb}$ (VPDB, ‰)	SD (‰)	$\delta^{18}O_{carb}$ (VPDB, ‰)	SD (‰)	Sample name	$\delta^{13}C_{carb}$ (VPDB, ‰)	SD (‰)	$\delta^{18}O_{carb}$ (VPDB, ‰)	SD (‰)
<u>Micrites</u>					3GZ153-M2	-3.77	0.02	-12.04	0.06
4GZ7-M2	-3.52	0.01	-5.65	0.01	3GZ173-M1	-3.63	0.02	-11.41	0.03
4GZ7-M3	-3.58	0.02	-5.88	0.03	3GZ173-M2	-3.86	0.03	-11.32	0.04
4GZ11-M1	-3.87	0.03	-4.53	0.01	3GZ173-M4	-3.45	0.02	-11	0.01
4GZ11-M2	-3.96	0.03	-4.51	0.05	<u>Vein/vug-fill calcites</u>				
4GZ18-M1	-3.76	0.04	-5.95	0.04	4GZ7-V1	-4.78	0.04	-13.24	0.04
4GZ18-M2	-3.89	0.02	-5.73	0.04	4GZ7-V4	-4.05	0.01	-10.15	0.05
4GZ79-M1	-3.77	0.02	-6.37	0.03	4GZ18-V3	-4.35	0.03	-11.01	0.01
4GZ79-M2	-3.94	0.04	-5.66	0.04	4GZ96-V3	-4.12	0.02	-13.89	0.02
4GZ79-M3	-3.91	0.03	-5.61	0.04	4GZ96-V4	-3.89	0.03	-13.8	0.01

4GZ96-M1	-3.64	0.01	-5.58	0.11	2GZ58-V1	-5.19	0.02	-12.95	0.02
4GZ96-M2	-3.37	0.02	-4.92	0.07	3GZ153-V3	-4.57	0.04	-14.74	0.03
2GZ58-M2	-5.62	0.01	-8.61	0.08	3GZ153-V4	-4.8	0.01	-14.31	0
3GZ153-M1	-4.25	0.01	-11.69	0.02	3GZ173-V3	-4.32	0.01	-14.05	0.09

Note: M indicates micrite; V indicates vein/vug-fill calcite; I, 2, 3, and 4 indicates different powder drilled from the same sample.

*See Fig. 1 for locations of sections 2GZ, 3GZ, and 4GZ.

Table 3. Summary of carbonate clumped isotope temperatures.

Sample name	Rep. no.	$\delta^{13}C_{carb}$ (VPBD/‰)	SD§ (‰)	$\delta^{18}O_{carb}$ (VPBD/‰)	SD§ (‰)	$\Delta 638_{CDES}$$^{\#}$ (‰)	SD§ (‰)	1 SE (‰)	95% conf.	Temp.^ (°C)	Error* (°C)	$\delta^{18}O_{w}$‡ (SMOW/‰)	Error (‰)
<u>Micrites</u>													
4GZ7	4	-3.65	0.01	-7.01	0.03	0.590	0.012	0.004	0.007	41.9	4.3	-2.68	0.76
4GZ11	5	-3.86	0.01	-4.40	0.02	0.572	0.015	0.004	0.007	49.2	4.6	-0.26	0.75

4GZ18	5	-3.78	0.03	-5.93	0.01	0.579	0.017	0.004	0.007	46.4	4.4	-2.44	0.74
4GZ79	5	-3.99	0.01	-6.09	0.01	0.569	0.005	0.004	0.007	50.3	4.6	-1.92	0.74
4GZ96	4	-3.59	0.01	-5.26	0.02	0.589	0.012	0.004	0.007	42.4	4.3	-1.20	0.76
3GZ153-1	3	-4.26	0.01	-12.00	0.02	0.624	0.015	0.004	0.007	29.5	3.8	-10.67	0.74
3GZ153-2	5	-4.10	0.01	-12.33	0.01	0.575	0.008	0.003	0.006	47.7	4.2	-7.71	0.71
3GZ173	5	-4.03	0.01	-11.32	0.03	0.592	0.010	0.004	0.007	41.1	4.2	-8.40	0.74
Vein/vug-fill calcites													
4GZ7-V	3	-4.20	0.00	-13.76	0.07	0.651	0.006	0.003	0.007	20.6	3.5	-12.29	0.73
4GZ11-V	5	-4.04	0.05	-7.42	0.28	0.620	0.012	0.003	0.006	30.8	3.7	-3.89	0.72
4GZ18-V	4	-4.10	0.02	-9.35	0.08	0.639	0.010	0.003	0.006	24.7	3.5	-7.03	0.71
4GZ96-V	3	-3.69	0.04	-11.16	0.17	0.617	0.010	0.004	0.007	30.4	3.9	-7.72	0.76
2GZ58-V	4	-5.97	0.02	-14.12	0.02	0.570	0.013	0.003	0.007	50.0	4.4	-7.13	0.76

3GZ153-V	5	-4.94	0.04	-14.69	0.14	0.572	0.014	0.003	0.006	49.0	4.2	-7.86	0.73

Notes: Rep. no., replicate number; SD, standard deviation; SE, standard error; 95% conf., 95% confidence interval; Temp., temperature.

[§] The SD is reported as analytical uncertainties, not including systematic uncertainties.

[#] In the new TILDAS system, Δ_{638} is equivalent to the conventional Δ_{47}. See method section 3.4 for more information.

^ The temperature calibration equation is: $\Delta_{638\mathrm{CDES}} = 0.0405\pm0.0006 \times (10^6/T^2) + 0.1822\pm0.0061$, $R^2 = 0.985$ (Yanay et al., 2022).

[*] The temperature error is calculated using the "pooled" standardization approach of Daëron (2021).

[‡] $\delta^{18}O_w$ values were calculated from Temp. and $\delta^{18}O_{carb}$ values using a linear combination of the dolomite calibration of Vasconcelos et al. (2005): $10^3\ln\alpha_{(\text{dolomite-water})} = (2.73 \times 10^6)/(T + 273.15)^2 + 0.26$; and calcite calibration of Kim and O'Neil (1997): $10^3\ln\alpha_{(\text{calcite-water})} = (18.03 \times 10^3)/(T + 273.15) - 32.42$, and relative abundance of calcite and dolomite based on X-ray diffraction results (Table 1).

Figure captions

Figure 1. (A) Shaded relief map of the Tibetan Plateau showing locations of major Cenozoic basins, including the Gerze area, along the Bangong suture zone in central Tibet. Abbreviations: JSS, Jinsha suture; BNS, Bangong-Nujiang suture; IYS, Indus-Yarlung suture; GSBT, Gerze-Seling Co backthrust; SGAT, Shiquanhe-Gerze-Amdo thrust. **(B)** Simplified geological map of the Gerze area showing locations of studied sections 2GZ, 3GZ, and 4GZ. The map is adapted from regional geological maps. **(C)** Satellite image of the 4GZ section and the section studied by Wei et al. (2016). Note that the two sections are located on the different limbs of a syncline.

Figure 2. Summary of criteria used to distinguish between different diagenetic stages. The graph is modified after Choquette and Pray (1970). Notes: 1) The timing of carbonate formation can be determined either using magnetostratigraphy or carbonate U-Pb dating; 2) The high and low formation temperatures are both within plausible Earth-surface temperatures; while the higher temperature indicates slightly higher than plausible Earth-surface temperatures, e.g., ~40 °C. 3) the timing depends on the sediment accumulation rate. 4) If only solid-state reordering occurred, the $\delta^{18}O_{carb}$ values would remain the same as primary; if closed-system recrystallization occurred, the $\delta^{18}O_{carb}$ values would be similar to primary, with only a slight difference; if open-system recrystallization occurred, the $\delta^{18}O_{carb}$ values would be much lower, due to high burial temperatures. 5) Slightly higher if only experienced partial solid-state reordering; but much higher if experienced total solid-state reordering or recrystallization, whether in closed or open systems. 6) assumed to occur at high elevations, considering exhumation due to contractional deformation. 7) the timing depends on the exhumation rate. 8) Slightly higher if still shallowly buried or low if exhumed to the surface at high elevation.

Figure 3. Representative petrographic images of the studied lacustrine carbonate samples. Also shown are the $\delta^{18}O_{carb}$ (VPDB) values. All images are under cross-polarized light (XPL).

Figure 4. EPMA maps of major elements (Ca, above; and Mg, below) of samples 4GZ11 (**A–B**), and 4GZ96 for both coarse-scale (**C–D**) and fine-scale (**E–F**).

Figure 5. Carbonate $\delta^{18}O_{carb}$ (VPDB) values (**A**), $\delta^{13}C_{carb}$ (VPDB) values (**B**), and paleotemperatures based on clumped isotope Δ_{638} (**C**) for the studied sections. (**D**) calculated $\delta^{18}O_{w}$ (VSMOW) values of paleo-meteoric water. Note that for sample 3GZ153, there are two separate Δ_{638} analyses with one analysis yielding a lower temperature of ~29 °C (circled; see text for discussion). The vertical axes are unitless and just used to distinguish different samples. The gray horizontal line separates 4GZ samples from the 2GZ/3GZ samples.

Figure 6. Results for solid-state reordering modeling. (A) for 30 °C dolomite experiencing maximum burial temperature of 170 °C, causing reordering to 49.1 °C; (B) for 30°C calcite experiencing maximum burial temperature of 142°C, causing reordering to 50.5 °C; (C) for 30 °C dolomite experiencing maximum burial temperature of 142 °C, causing slight reordering to 33.5°C; (D) for 30°C calcite experiencing maximum burial temperature of 170°C, causing reordering to 87.4 °C.

Figure 7. Carbonate LA-ICPMS U-Pb dating of the vein/vug-fill calcites of sample 4GZ96, depicted using a Tera-Wasserburg plot (Tera and Wasserburg, 1972). The two individual analyses are made on two separate slabs containing vein/vug-fill calcites of the same sample.

Figure 8. Carbonate U and Th content analyzed using LA-ICPMS method.

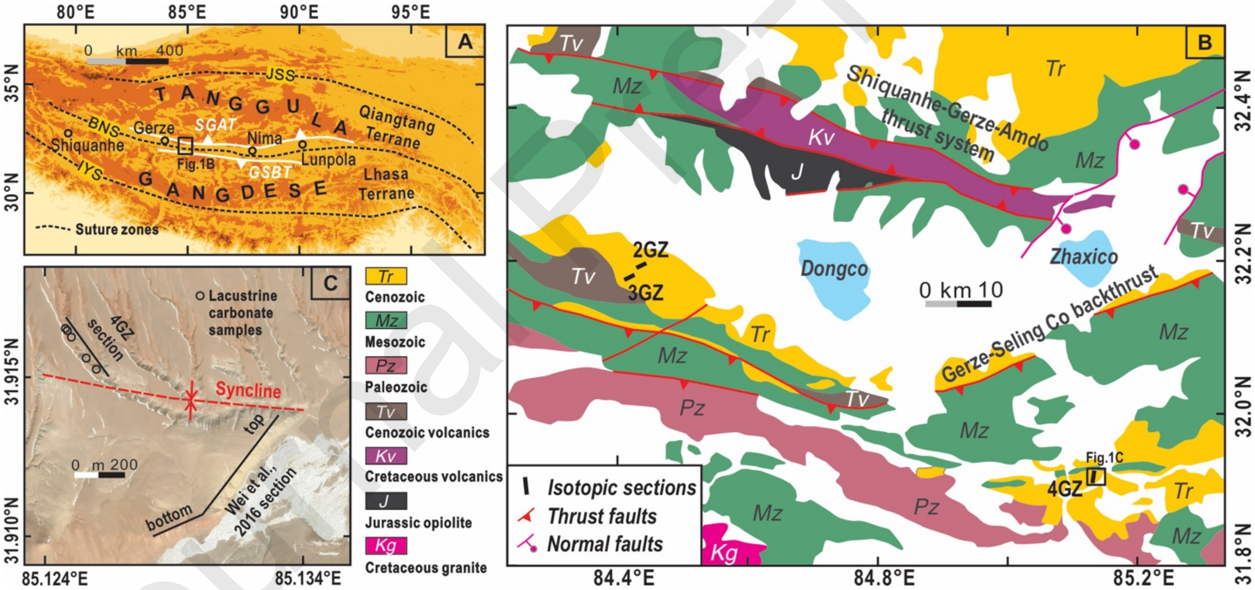

Figure 1

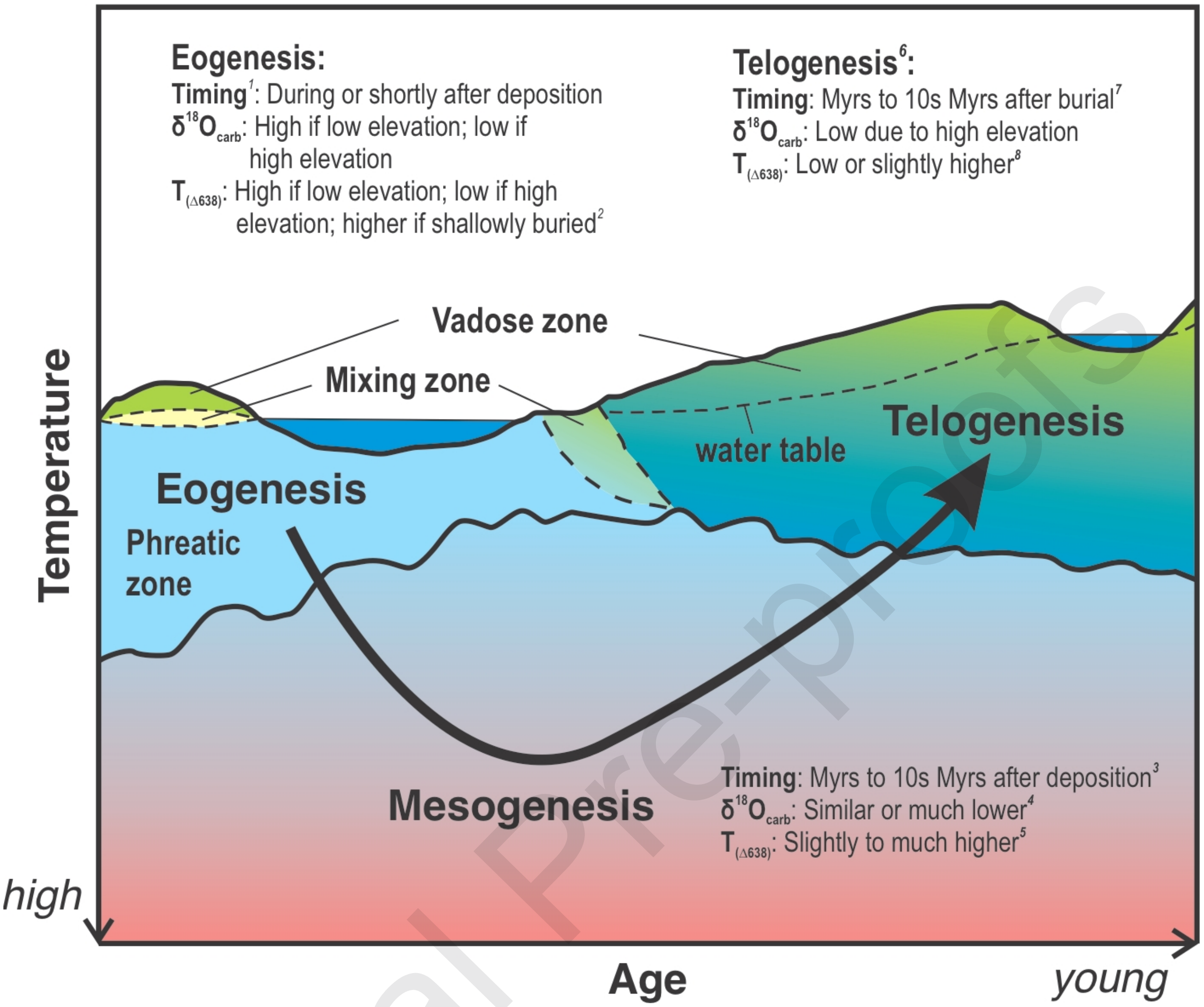
Eogenesis:
Timing[1]: During or shortly after deposition
δ^{18}O$_{carb}$: High if low elevation; low if high elevation
T$_{(\Delta 638)}$: High if low elevation; low if high elevation; higher if shallowly buried[2]
Telogenesis[6]:
Timing: Myrs to 10s Myrs after burial[7]
δ^{18}O$_{carb}$: Low due to high elevation
T$_{(\Delta 638)}$: Low or slightly higher[8]
Vadose zone
Mixing zone
water table
Telogenesis
Eogenesis
Phreatic zone
Mesogenesis
Timing: Myrs to 10s Myrs after deposition[3]
δ^{18}O$_{carb}$: Similar or much lower[4]
T$_{(\Delta 638)}$: Slightly to much higher[5]
Temperature
high
Age
young

Figure 2

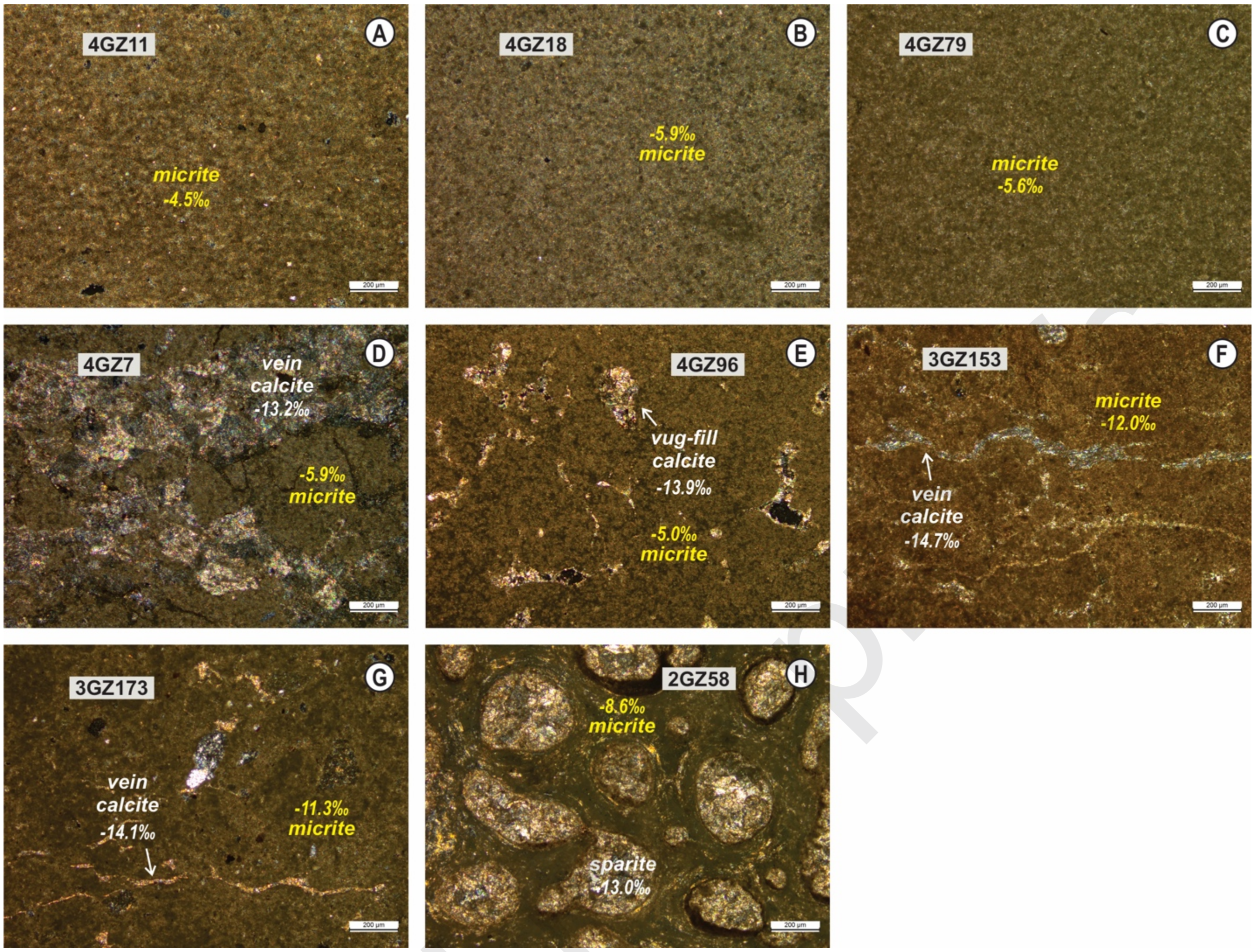
4GZ11
A
micrite
-4.5‰
200 µm
4GZ18
B
-5.9‰
micrite
200 µm
4GZ79
C
micrite
-5.6‰
200 µm
4GZ7
D
vein
calcite
-13.2‰
-5.9‰
micrite
200 µm
4GZ96
E
vug-fill
calcite
-13.9‰
-5.0‰
micrite
200 µm
3GZ153
F
micrite
-12.0‰
vein
calcite
-14.7‰
200 µm
3GZ173
G
vein
calcite
-14.1‰
-11.3‰
micrite
200 µm
2GZ58
H
-8.6‰
micrite
sparite
-13.0‰
200 µm

Figure 3

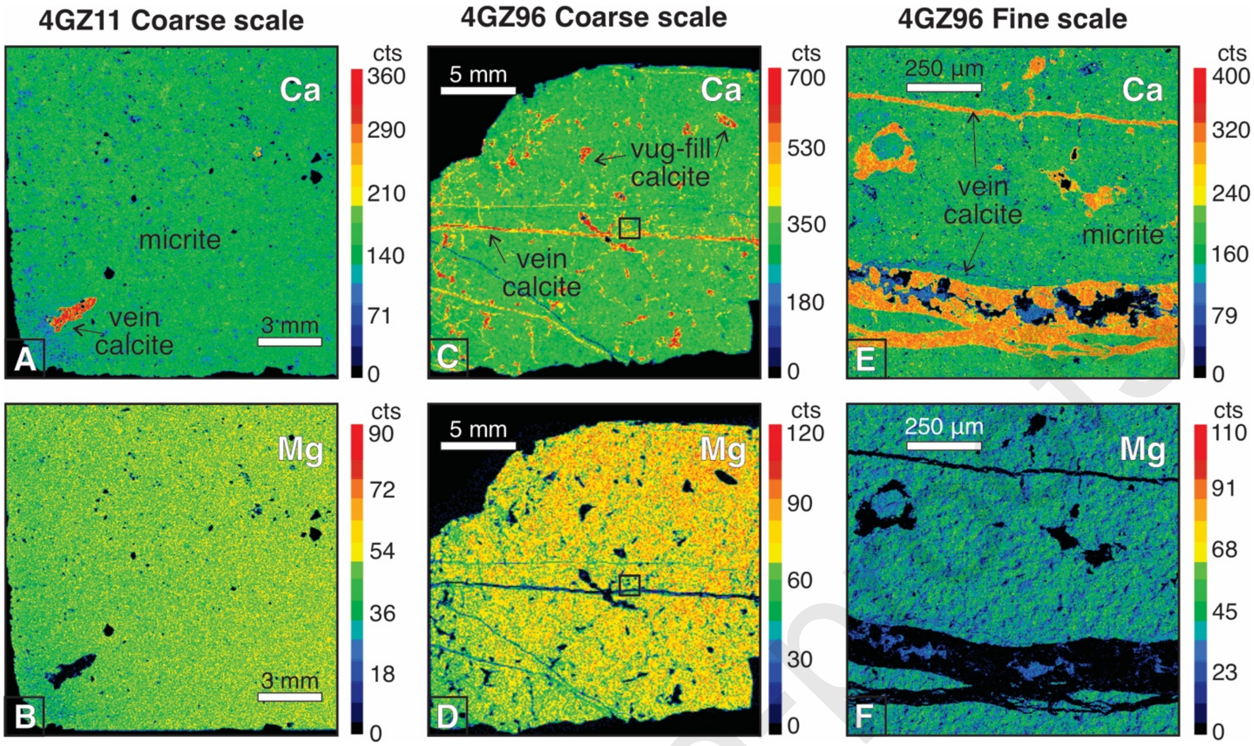
4GZ11 Coarse scale
4GZ96 Coarse scale
4GZ96 Fine scale
Ca
Mg
micrite
vein calcite
vug-fill calcite
3 mm
5 mm
250 µm
cts
360
290
210
140
71
0
700
530
350
180
0
400
320
240
160
79
0
90
72
54
36
18
0
120
90
60
30
0
110
91
68
45
23
0
A
B
C
D
E
F

Figure 4

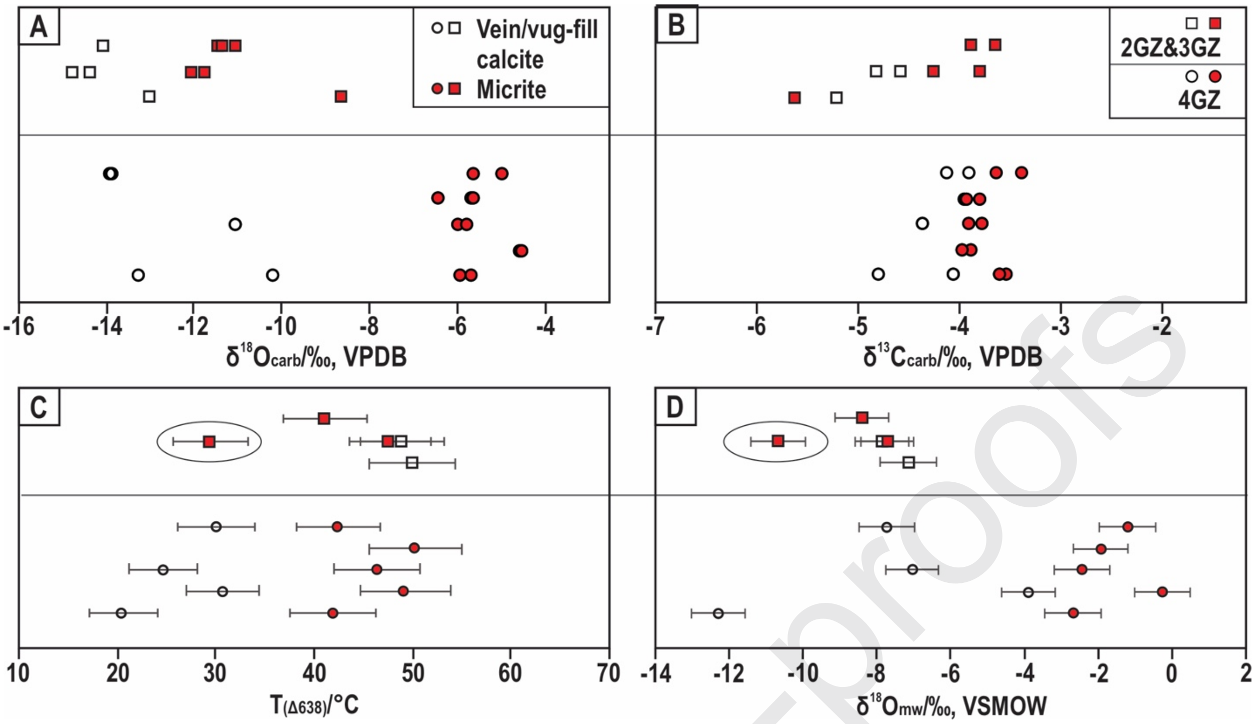
A
B
C
D
Vein/vug-fill calcite
Micrite
2GZ&3GZ
4GZ
-16 -14 -12 -10 -8 -6 -4
δ18Ocarb/‰, VPDB
-7 -6 -5 -4 -3 -2
δ13Ccarb/‰, VPDB
10 20 30 40 50 60 70
T(Δ638)/°C
-14 -12 -10 -8 -6 -4 -2 0 2
δ18Omw/‰, VSMOW

Figure 5

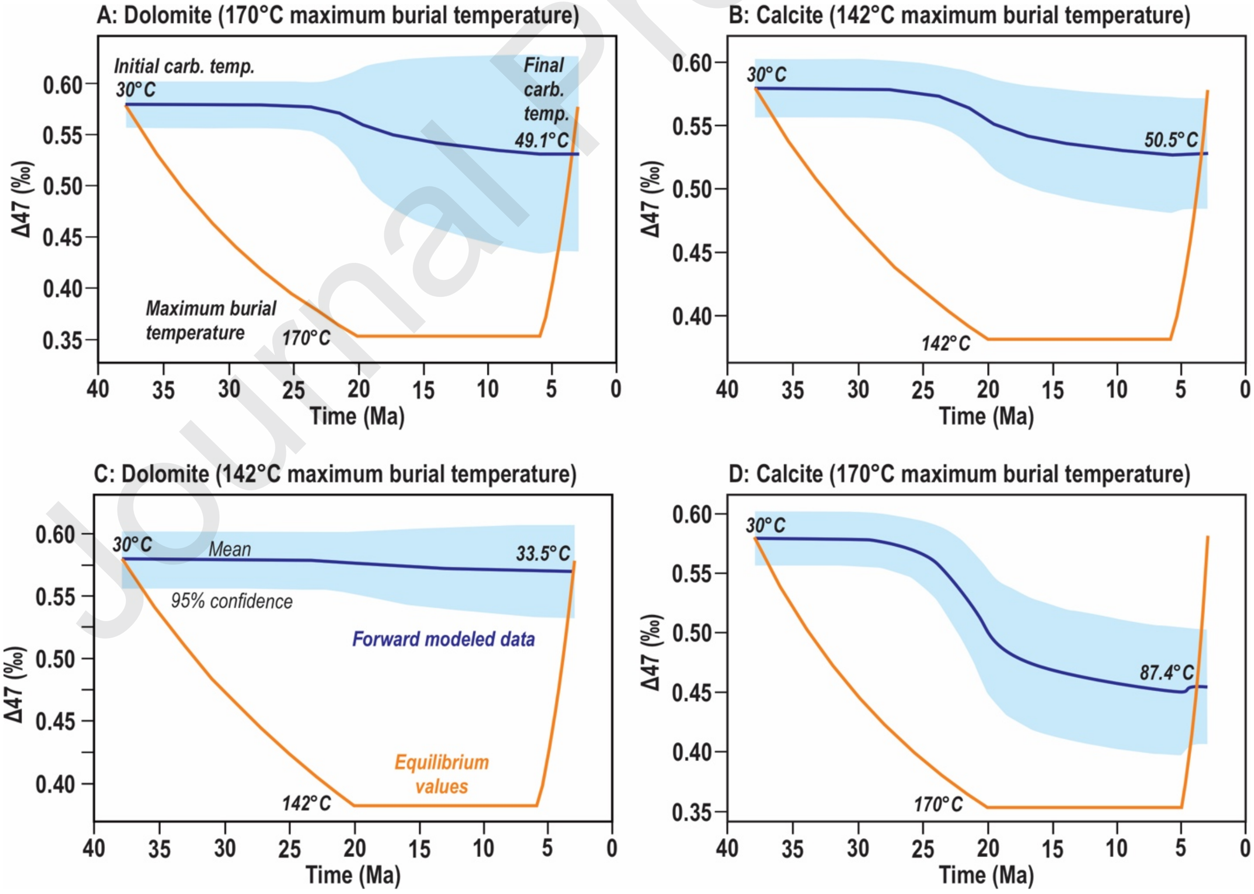
A: Dolomite (170°C maximum burial temperature)
Initial carb. temp.
30°C
Final carb. temp.
49.1°C
Maximum burial temperature
170°C
B: Calcite (142°C maximum burial temperature)
30°C
50.5°C
142°C
C: Dolomite (142°C maximum burial temperature)
30°C
Mean
33.5°C
95% confidence
Forward modeled data
Equilibrium values
142°C
D: Calcite (170°C maximum burial temperature)
30°C
87.4°C
170°C
Δ47 (‰)
0.60 0.55 0.50 0.45 0.40 0.35
Time (Ma)
40 35 30 25 20 15 10 5 0

Figure 6

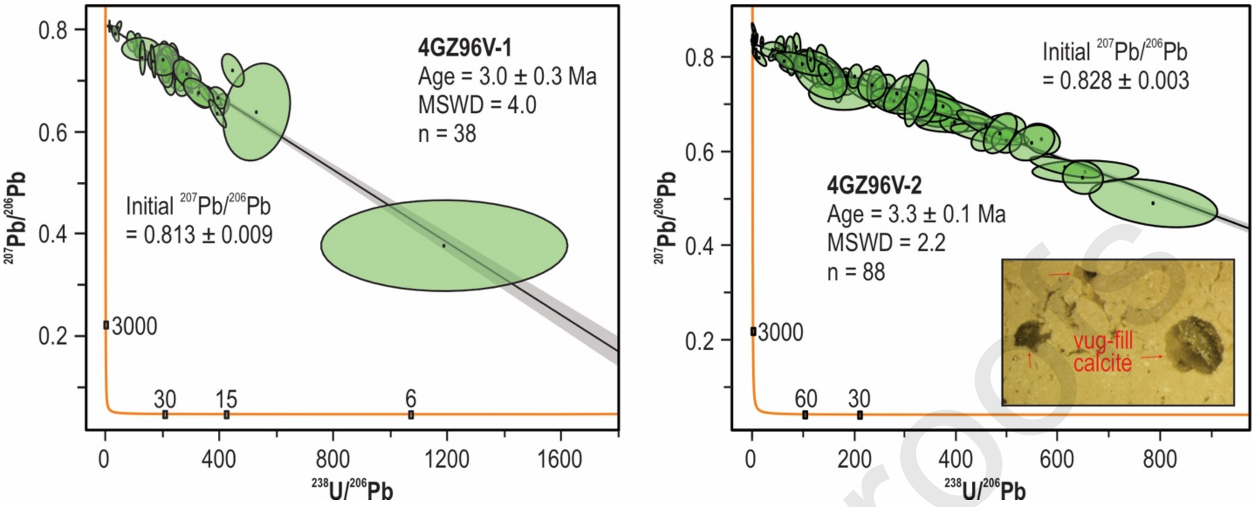

Figure 7

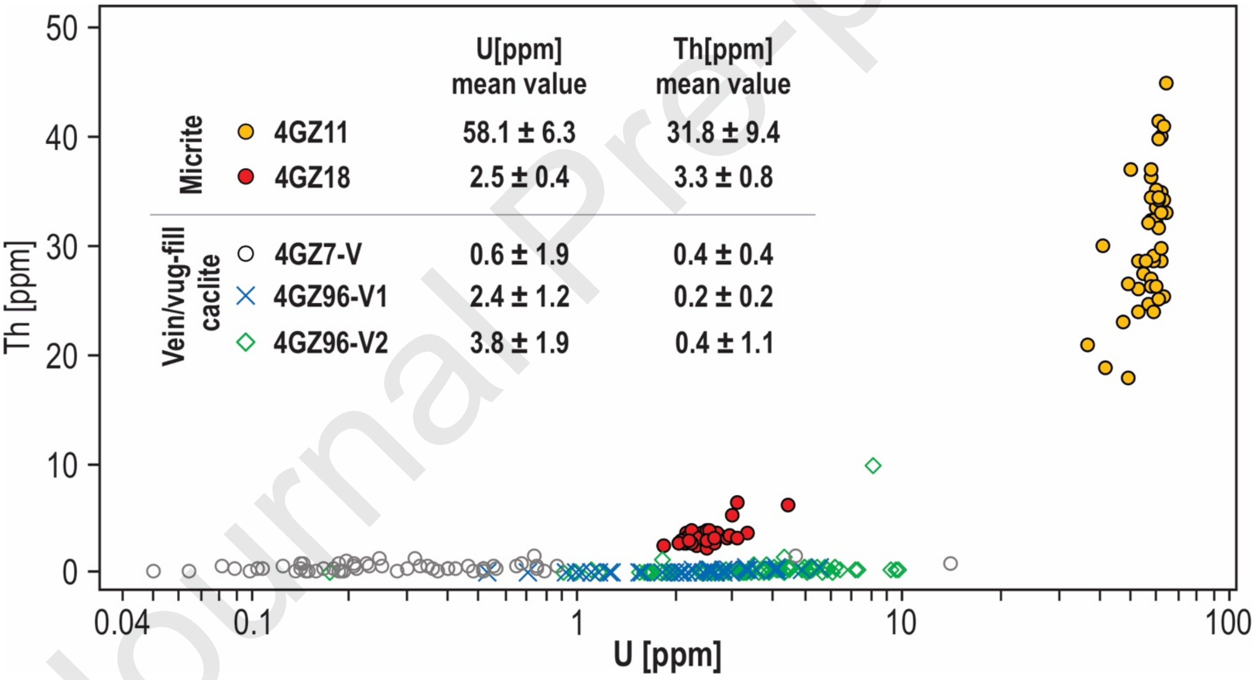

Figure 8

Declaration of interests

☒ The authors declare that they have no known competing financial interests or personal relationships that could have appeared to influence the work reported in this paper.

☐The authors declare the following financial interests/personal relationships which may be considered as potential competing interests: